The Astrophysical Journal, 904:130 (20pp), 2020 December 1 https://doi.org/10.3847/1538-4357/abc563

Kiloparsec-scale ALMA Imaging of [C II] and Dust Continuum Emission of 27 Quasar Host Galaxies at $z \sim 6$

Bram P. Venemans[1], Fabian Walter[1,2], Marcel Neeleman[1], Mladen Novak[1], Justin Otter[1,3], Roberto Decarli[4], Eduardo Bañados[1], Alyssa Drake[1], Emanuele Paolo Farina[5], Melanie Kaasinen[1], Chiara Mazzucchelli[6], Chris Carilli[2], Xiaohui Fan[7], Hans-Walter Rix[1], and Ran Wang[8]
[1] Max-Planck Institute for Astronomy, Königstuhl 17, D-69117 Heidelberg, Germany; venemans@mpia.de
[2] National Radio Astronomy Observatory, Pete V. Domenici Array Science Center, P.O. Box 0, Socorro, NM 87801, USA
[3] Department of Physics & Astronomy, Johns Hopkins University, Bloomberg Center, 3400 N Charles St., Baltimore, MD 21218, USA
[4] INAF—Osservatorio di Astrofisica e Scienza dello Spazio di Bologna, via Gobetti 93/3, I-40129, Bologna, Italy
[5] Max Planck Institut für Astrophysik, Karl–Schwarzschild–Straße 1, D-85748, Garching bei München, Germany
[6] European Southern Observatory, Alonso de Córdova 3107, Vitacura, Región Metropolitana, Chile
[7] Steward Observatory, University of Arizona, 933 N Cherry Ave, Tucson, AZ 85719, USA
[8] Kavli Institute for Astronomy and Astrophysics, Peking University, No. 5 Yiheyuan Road, Haidian District, Beijing, 100871, People's Republic of China
Received 2020 July 17; revised 2020 October 5; accepted 2020 October 23; published 2020 November 27

Abstract

We present a study of the [C II] 158 μm line and underlying far-infrared (FIR) continuum emission of 27 quasar host galaxies at $z \sim 6$, traced by the Atacama Large Millimeter/submillimeter Array at a spatial resolution of $\sim$1 physical kpc. The [C II] emission in the bright, central regions of the quasars have sizes of 1.0–4.8 kpc. The dust continuum emission is typically more compact than [C II]. We find that 13/27 quasars (approximately one-half) have companion galaxies in the field, at projected separations of 3–90 kpc. The position of dust emission and the Gaia-corrected positions of the central accreting black holes are cospatial (typical offsets $\lesssim 0\farcs1$). This suggests that the central black holes are located at the bottom of the gravitational wells of the dark matter halos in which the $z > 6$ quasar hosts reside. Some outliers with offsets of $\sim$500 pc can be linked to disturbed morphologies, most likely due to ongoing or recent mergers. We find no correlation between the central brightness of the FIR emission and the bolometric luminosity of the accreting black hole. The FIR-derived star formation rate densities (SFRDs) in the host galaxies peak at the galaxies' centers, at typical values between 100 and 1000 $M_\odot\,\mathrm{yr}^{-1}\,\mathrm{kpc}^{-2}$. These values are below the Eddington limit for star formation, but similar to those found in local ultraluminous infrared galaxies. The SFRDs drop toward larger radii by an order of magnitude. Likewise, the [C II]/FIR luminosity ratios of the quasar hosts are lowest in their centers (few $\times 10^{-4}$) and increase by a factor of a few toward the galaxies' outskirts, consistent with resolved studies of lower-redshift sources.

Unified Astronomy Thesaurus concepts: Observational cosmology (1146); High-redshift galaxies (734); Quasars (1319); Star formation (1569)

1. Introduction

Luminous quasars at high redshift, $z \gtrsim 6$, are extreme astrophysical objects. Accretion onto their central supermassive black holes with masses exceeding $10^9\,M_\odot$ (e.g., De Rosa et al. 2014; Mazzucchelli et al. 2017; Shen et al. 2019) results in extremely bright emission in the rest-frame ultraviolet bands (absolute magnitudes up to $M_{\rm UV} > -29$; see, e.g., Wu et al. 2015). This means that even the most distant quasars currently known at $z = 7.5$ (Bañados et al. 2018; Yang et al. 2020) can be detected with a 4 m class near-infrared telescope in a few minutes.

Similarly, it has been demonstrated that the galaxies that harbor the central supermassive black holes can also be very luminous in the rest-frame far-infrared (FIR). The [C II] emission line, one of the main coolants of the interstellar medium (ISM), and the underlying dust continuum emission can be detected with state-of-the-art millimeter facilities, such as the Atacama Large Millimeter/submillimeter Array (ALMA) and the NOrthern Extended Millimeter Array (NOEMA), in less than an hour (e.g., Decarli et al. 2018; Yang et al. 2019). The global [C II] and dust properties of the host galaxies of a large sample of luminous $z \sim 6$ quasars with central black holes with masses $\gtrsim 10^9\ M_\odot$ were recently presented in Decarli et al. (2018) and Venemans et al. (2018). In general, the [C II] emission in these quasar host galaxies has a luminosity in the range 10^9–$10^{10}\ L_\odot$, from which Decarli et al. (2018) infer star formation rates (SFRs) of $\sim$200–2000 $M_\odot\,\mathrm{yr}^{-1}$. Based on the detection of the dust emission, Venemans et al. (2018) derived FIR luminosities of $L_{\rm FIR} > 10^{12}\,L_\odot$ for the majority of quasar hosts and high dust masses of 10^7–$10^9\ M_\odot$. The host galaxies of distant quasars thus provide a unique opportunity to study the formation and build-up of massive galaxies in the early universe in detail.

One of the surprising results of the FIR imaging of distant quasar host galaxies was the discovery of massive, gas-rich companion galaxies within 60 kpc and 600 $\mathrm{km\,s}^{-1}$ of the quasar (Wang et al. 2011; Decarli et al. 2017; Willott et al. 2017; Neeleman et al. 2019; Venemans et al. 2019). Similar gas-rich galaxies have been discovered around luminous quasars at slightly lower redshift, $z \sim 5$ (e.g., Trakhtenbrot et al. 2017; Nguyen et al. 2020). The fraction of quasars that show at least one nearby galaxy at a similar redshift is at least 15%–30% (Decarli et al. 2017; Nguyen et al. 2020), indicating that major mergers might play a significant role in triggering these luminous quasars, in contrast to (some) studies at lower redshifts ($z \sim 2$, e.g., Marian et al. 2019). However, signatures of ongoing or recent merging events in high-redshift quasar host galaxies have been rarely observed (e.g., Bañados et al. 2019;

Decarli et al. 2019; Venemans et al. 2019), mostly due to the limited spatial resolution of the FIR observations.

So far, millimeter facilities have observed a small sample of quasar host galaxies at high-enough spatial resolution to resolve the emission of the quasar host galaxies. Despite the small number of targets, there appears to be a surprising variety in the morphology of gas and dust emission (e.g., Walter et al. 2009; Shao et al. 2017; Neeleman et al. 2019; Venemans et al. 2017a, 2019). Some objects show very compact ($<$1.5 kpc) dispersion-dominated emission, with implied high central gas densities and star formation surface densities (e.g., Venemans et al. 2017a; Neeleman et al. 2019). Others show more extended disk-like, rotation-dominated [C II] emission, distributed over many kpc^2 (e.g., Wang et al. 2013; Shao et al. 2017; Pensabene et al. 2020). In other cases, the [C II] emission does not show ordered rotation, but rather a very disturbed morphology, possibly due to interaction with nearby galaxies (e.g., Decarli et al. 2019; Venemans et al. 2019). These vastly different morphologies and gas kinematics could provide insights into early black hole growth (i.e., is the accretion onto the central black hole related to whether or not the gas kinematics are disturbed in the central region of the host galaxy?).

We therefore initiated a comprehensive study of $z \sim 6$ quasar host galaxies using all available high-spatial-resolution FIR observations to probe the gas and dust on scales of $\sim$1 kpc. The main goals of this study are to (1) determine the morphology, size, and kinematics of the [C II]-emitting region and of the continuum emission in order to differentiate between different merger states and to constrain the dynamical mass of quasar hosts; (2) resolve the FIR surface density on kiloparsec scales to determine whether the central active galactic nucleus (AGN) plays a role in the heating of the dust; and (3) accurately measure the profile and extent of the [C II] emission to explore the presence of possible gas infall or outflows.

These goals will be addressed in three parallel papers. In this paper, the first of the series, we will outline the sample and present new and archival high-spatial-resolution ALMA observations of $z \sim 6$ quasar host galaxies. We will discuss the global properties of the sample, study the size and morphology of the gas and dust emission, and examine the environment. In another paper of the series, Novak et al. (2020) investigate the presence of large-scale spatial features in the [C II] and dust emission and constrain the broad spectral features in the [C II] emission line to look for evidence of gas outflows. In a third paper, M. Neeleman et al. (2020 in preparation) analyze the kinematics of the [C II] emission in the quasar hosts and constrain the dynamical mass of the galaxies. They further investigate the relation between the dynamical mass of the quasar host galaxies and the mass of the central black hole.

This paper is organized as follows. In Section 2, we introduce the sample of high-redshift quasar host galaxies analyzed in this paper (Section 2.1) and provide the details of the observations and reduction (Section 2.2). In Section 3 we present our main results, from the spectra (Section 3.1), the moment-zero maps (Section 3.2), and from the search for line emitters in the field (Section 3.3). Our results are discussed in Section 4, followed by a summary in Section 5.

We adopt a concordance cosmology with $\Omega_M = 0.3$, $\Omega_\Lambda = 0.7$, and $H_0 = 70$ km s^{-1} Mpc^{-1}, which is consistent with the recent measurements of Planck (Planck Collaboration et al. 2016). In this cosmology at a redshift of 6.0 (7.0), 1″ corresponds to 5.7 (5.2) kpc. Star formation rates are computed using the Kroupa & Weidner (2003) initial mass function.

2. Observations

2.1. Sample

The sample presented in this paper consists of all quasars at $z > 5.7$ for which high spatial resolution (here defined as a spatial resolution better than $\sim$0.″35, or $\lesssim$2 kpc) was obtained with ALMA up to the end of Cycle 6 (2019 September). In total, 27 quasars were found to have sufficiently high spatial resolution ALMA imaging. Note that this sample of $z \sim 6$ quasars is different from the one presented in Decarli et al. (2018) and Venemans et al. (2018), despite containing the same number of objects. The quasars and the details of the observations are listed in Table 1. In Appendix A we describe some individual objects in more detail. The coordinates in the table represent the position of the optical/near-infrared point source (the active galactic nucleus); see Section 2.3 for the details. All quasars in our sample have previously been detected in the redshifted [C II] emission and far-infrared continuum, mostly in low-resolution imaging (with beam sizes $\gtrsim$0.″7; e.g., Decarli et al. 2018). In Figure 1 we show the redshift and [C II] luminosity distribution of our sample.

2.2. ALMA Observations and Data Reduction

The ALMA data presented in this paper were obtained as part of several projects observed between Cycle 1 and Cycle 6. The project IDs are 2012.1.00240.S (PI: R. Wang), 2012.1.00882.S (PI: B. Venemans), 2013.1.00273.S (PI: B. Venemans), 2015.1.00399.S (PI: B. Venemans), 2015.1.00692.S (PI: X. Fan), 2016.1.00544 (PI: E. Bañados), 2016.A.00018.S (PI: R. Decarli), 2017.1.00396.S (PI: E. Bañados), 2017.1.01301.S (PI: F. Walter), and 2018.1.00908.S (PI: F. Walter); see Table 1. The observations were carried out between 2013 July 5 and 2019 September 24. The on-source integration time for each data set ranged from 16 to 161 min, and the spatial resolution varies from 0.″1 to 0.″33. The number of antennas was 34 to 49 (see Table 1 for details). The beam size listed in Table 1 is that in the [C II] maps, created with ROBUST = 0.5 weighting (see below).

The setup of the observations differed slightly from source to source, but for most sources two overlapping sidebands (SPWs), 1.875 GHz wide each, were used to cover the redshifted [C II] line (rest frequency of 1900.54 GHz). The frequency coverage around the [C II] line in these cases was about 3.3 GHz, which corresponds to $\sim$3600 km s^{-1} at $z = 6$. Two other bandpasses of 1.875 GHz each were placed $\sim$15 GHz away, probing only continuum emission.

The data were reduced following the standard reduction steps using the Common Astronomy Software Applications package (CASA; McMullin et al. 2007). The calibration of the data was performed using the standard pipeline, with a few exceptions. For details on the data reduction and calibration, we refer to the accompanying paper by Novak et al. (2020). The reduced measurement sets were subsequently imaged using the CASA task TCLEAN using Briggs weighting with the robust parameter set to ROBUST = 0.5. This value optimizes both signal-to-noise ratio (S/N) and spatial resolution. For all cubes and maps, we cleaned down to 2σ with σ being the rms noise.

Table 1
Characteristics of the $z > 5.7$ Quasar Sample and the ALMA Observations

Name	R.A. (ICRS)[a]	Decl. (ICRS)[a]	ΔR.A. × ΔDecl.[a]	Project ID	$t_{\rm on-source}$[b] (min.)	$n_{\rm ant}$[c]	Beam[d]	rms per 30 MHz (mJy beam^{-1})
P007+04	$00^{\rm h}28^{\rm m}06\overset{\rm s}{.}568$	+04°57′25.″39	0.″04 × 0.″05	2017.1.01301.S	29	44	0.″26 × 0.″22	0.25
P009–10	$00^{\rm h}38^{\rm m}56\overset{\rm s}{.}519$	−10°25′53.″97	0.″04 × 0.″04	2017.1.01301.S	26	44	0.″32 × 0.″22	0.54
J0100+2802	$01^{\rm h}00^{\rm m}13\overset{\rm s}{.}025$	+28°02′25.″80	0.″03 × 0.″02	2015.1.00692.S	72	44	0.″24 × 0.″12	0.18
J0109–3047	$01^{\rm h}09^{\rm m}53\overset{\rm s}{.}136$	−30°47′26.″30	0.″02 × 0.″05	2013.1.00273.S	36	40	0.″20 × 0.″17	0.20
				2015.1.00399.S	32	41		
J0129–0035	$01^{\rm h}29^{\rm m}58\overset{\rm s}{.}515$	−00°35′39.″81	0.″03 × 0.″03	2012.1.00240.S	76	37–41	0.″22 × 0.″16	0.22
J025–33	$01^{\rm h}42^{\rm m}43\overset{\rm s}{.}720$	−33°27′45.″61	0.″06 × 0.″10	2017.1.01301.S	24	44	0.″24 × 0.″21	0.27
P036+03	$02^{\rm h}26^{\rm m}01\overset{\rm s}{.}873$	+03°02′59.″24	0.″04 × 0.″03	2015.1.00399.S	75	41–42	0.″15 × 0.″12	0.18
J0305–3150	$03^{\rm h}05^{\rm m}16\overset{\rm s}{.}918$	−31°50′55.″85	0.″01 × 0.″04	2013.1.00273.S	16	34	0.″18 × 0.″15	0.26
				2015.1.00399.S	38	44		
P065–26	$04^{\rm h}21^{\rm m}38\overset{\rm s}{.}050$	−26°57′15.″72	0.″05 × 0.″06	2017.1.01301.S	25	47	0.″29 × 0.″21	0.32
J0842+1218	$08^{\rm h}42^{\rm m}29\overset{\rm s}{.}438$	+12°18′50.″47	0.″03 × 0.″02	2016.1.00544.S	54	42	0.″27 × 0.″23	0.28
J1044–0125	$10^{\rm h}44^{\rm m}33\overset{\rm s}{.}040$	−01°25′02.″08	0.″01 × 0.″01	2012.1.00240.S	76	34–35	0.″22 × 0.″16	0.39
J1048–0109	$10^{\rm h}48^{\rm m}19\overset{\rm s}{.}077$	−01°09′40.″42	0.″02 × 0.″01	2017.1.01301.S	26	43	0.″27 × 0.″23	0.24
P167–13	$11^{\rm h}10^{\rm m}33\overset{\rm s}{.}963$	−13°29′45.″73	0.″07 × 0.″04	2016.1.00544.S	43	47	0.″33 × 0.″22	0.20
J1120+0641	$11^{\rm h}20^{\rm m}01\overset{\rm s}{.}463$	+06°41′23.″79	0.″02 × 0.″03	2012.1.00882.S	161	38–47	0.″24 × 0.″23	0.13
P183+05	$12^{\rm h}12^{\rm m}26\overset{\rm s}{.}969$	+05°05′33.″49	0.″05 × 0.″02	2016.1.00544.S	47	39	0.″27 × 0.″24	0.32
J1306+0356	$13^{\rm h}06^{\rm m}08\overset{\rm s}{.}259$	+03°56′26.″19	0.″02 × 0.″02	2017.1.01301.S	28	43	0.″25 × 0.″24	0.45
J1319+0950	$13^{\rm h}19^{\rm m}11\overset{\rm s}{.}291$	+09°50′51.″49	0.″02 × 0.″01	2012.1.00240.S	50	34	0.″27 × 0.″21	0.29
J1342+0928	$13^{\rm h}42^{\rm m}08\overset{\rm s}{.}100$	+09°28′38.″36	0.″17 × 0.″10	2017.1.00396.S	114	43	0.″20 × 0.″15	0.13
P231–20	$15^{\rm h}26^{\rm m}37\overset{\rm s}{.}844$	−20°50′00.″88	0.″08 × 0.″08	2016.1.00544.S	43	44	0.″21 × 0.″12	0.21
P308–21	$20^{\rm h}32^{\rm m}09\overset{\rm s}{.}996$	−21°14′02.″38	0.″08 × 0.″08	2016.A.00018.S	56	44–45	0.″28 × 0.″22	0.17
J2054–0005	$20^{\rm h}54^{\rm m}06\overset{\rm s}{.}496$	−00°05′14.″57	0.″10 × 0.″10	2018.1.00908.S	85	46	0.″15 × 0.″11	0.28
J2100–1715	$21^{\rm h}00^{\rm m}54\overset{\rm s}{.}698$	−17°15′22.″00	0.″06 × 0.″06	2017.1.01301.S	25	45	0.″24 × 0.″20	0.38
P323+12	$21^{\rm h}32^{\rm m}33\overset{\rm s}{.}178$	+12°17′55.″07	0.″02 × 0.″05	2018.1.00908.S	43	49	0.″12 × 0.″09	0.29
J2318–3113	$23^{\rm h}18^{\rm m}18\overset{\rm s}{.}369$	−31°13′46.″42	0.″06 × 0.″04	2017.1.01301.S	24	45	0.″25 × 0.″22	0.33
J2318–3029	$23^{\rm h}18^{\rm m}33\overset{\rm s}{.}099$	−30°29′33.″58	0.″04 × 0.″03	2018.1.00908.S	40	48	0.″10 × 0.″10	0.20
J2348–3054	$23^{\rm h}48^{\rm m}33\overset{\rm s}{.}352$	−30°54′10.″35	0.″07 × 0.″09	2015.1.00399.S	52	44	0.″18 × 0.″14	0.25
P359–06	$23^{\rm h}56^{\rm m}32\overset{\rm s}{.}452$	−06°22′59.″31	0.″08 × 0.″04	2017.1.01301.S	26	44	0.″25 × 0.″21	0.27

Notes.
[a] Optical/near-infrared quasar position and uncertainty (see Section 2.3 for details).
[b] On-source integration time.
[c] Number of antennas.
[d] Beam size measured in the integrated [C II] maps.

For each quasar, we created the several data sets produced by the following procedure:

1. We first created two data cubes for each quasar field with a channel width of 30 MHz (corresponding to 32–40 km s^{-1}, depending on the redshift of the source), one covering the two bandpasses around the [C II] line and one covering the bandpasses ∼15 GHz away from the line. For J0109–3047 and J0305–3150, we created three data cubes as the continuum bandpasses were placed differently in Cycle 2 and Cycle 3 (Table 1), resulting in a total of 56 data cubes. The data cube containing the [C II] emission line was subsequently used to extract the total spectrum of the quasar host galaxy (see Section 3.1). In all 56 data cubes, we searched for emission line galaxies in the field (see Section 3.3). The rms in the bandpasses containing the redshifted [C II] line ranged from 0.13 to 0.54 mJy beam^{-1} per 30 MHz channel (Table 2.1).
2. We subtracted the continuum in *uv* space using the task UVCONTSUB with the polynomial order of the fit set to FITORDER = 1. The continuum was defined as all channels in two bandpasses surrounding the [C II] line that were at least 1.25 × FWHM of the [C II] line away from the peak of the line.
3. From the continuum-subtracted measurement sets, we created [C II] data cubes to analyze the kinematics of the emission line (discussed in M. Neeleman et al. 2020, in preparation).
4. [C II] intensity maps were created by averaging the channels 1.2 × FWHM around the peak of the [C II] line. This width results in the highest S/N [C II] map if the emission line is Gaussian (and the noise is constant); see Novak et al. (2020). The line flux in such a map is ∼84% of the total flux. The maps are presented in Section 3.2.
5. We created maps of the continuum emission by setting the deconvolver in TCLEAN to MTMFS (multiterm, multifrequency synthesis) with the number of Taylor coefficients set to two and the redshifted frequency of the [C II] line as reference frequency. The continuum in this step was defined as all channels in all four bandpasses that were at least 1.25 × FWHM away from the peak of the [C II] line. This procedure creates continuum maps at the frequency of the [C II] emission line by fitting a second-order polynomial to the continuum channels.

2.3. Optical/Near-infrared Coordinates

To compare the location of the accreting black hole (the quasar) to that of the host galaxy as traced by ALMA, we

required accurate positions of the optical/near-infrared quasar on the same reference frame as the ALMA observations. The optical or near-infrared positions of the quasars were taken from catalogs of large surveys such as the Pan-STARRS1 survey (Chambers et al. 2016) and the near-infrared VIKING survey (Edge et al. 2013). We corrected the position of stars within 2′ of the quasar in the optical/near-infrared catalogs that had a match in the Gaia DR2 catalog (Gaia Collaboration et al. 2018). To compute the uncertainty of these astrometrically corrected positions, we calculated the standard deviation of the offsets between the corrected and Gaia position of stars close to the quasar. The resulting uncertainties in the astrometry range from 0.″01 to 0.″15. The optical/near-infrared positions and the uncertainties are listed in Table 1. It should be noted that the position and uncertainties in the table do not account for systematic offsets that are due to differential chromatic refraction (see, e.g., Kaczmarczik et al. 2009). Because the refractive index of air is dependent on the wavelength, the difference in color of the quasars with respect to those of the stars used for the astrometric calibration could result in a systematic positional offset, especially if a quasar has been observed at high air mass. We will discuss this effect in Section 4.1.

3. Results

3.1. [C II] Spectra

To obtain a total spectrum of each quasar host galaxy, we extracted spectra in the [C II]+continuum data cubes. As our sources are all resolved at the spatial resolution of our observations, the emission could be extended over multiple beams. To obtain a full spectrum of a resolved source, we extracted spectra in an aperture while taking both clean and uncleaned (residual) components into account by applying the residual scale method. This method is described in detail in Novak et al. (2019, 2020). The apertures used for the extraction were chosen manually after visual inspection and had radii between 0.″4 and 1.″5, depending on the extent of the source (see Figure 3). The spectra for our 27 sources are shown in Figure 2.

We fitted a single Gaussian with a constant continuum to each of the extracted spectra. The fits are shown with red lines in Figure 2. The best-fit parameters are subsequently used to derive the properties of the [C II] line and FIR continuum in the quasar host. The measured [C II] redshift, line flux, line width, equivalent width, and continuum flux density are listed in Table 2. The equivalent width of the [C II] emission was computed via

$$\mathrm{EW}_{[\mathrm{CII}]}/\mu\mathrm{m} = 1000\,\frac{F_{[\mathrm{CII}]}}{S_{1900\,\mathrm{GHz}}}\,\frac{\lambda_{[\mathrm{CII}],0}}{c}, \quad (1)$$

with $F_{[\mathrm{CII}]}$ being the observed [C II] flux in Jy km s^{-1}, $S_{1900\,\mathrm{GHz}}$ the observed continuum flux density at a rest-frame frequency of 1900 GHz in mJy, and $\lambda_{[\mathrm{CII}],0}$ the rest wavelength of the [C II] emission line of $\lambda_{[\mathrm{CII}],0} = 157.74\,\mu$m. The [C II] luminosities were derived from the measured line fluxes using

$$L_{[\mathrm{CII}]}/L_\odot = 1.04 \times 10^{-3}\,\nu_{[\mathrm{CII}],\mathrm{obs}}\,F_{[\mathrm{CII}]}\,D_L^2, \quad (2)$$

with $\nu_{[\mathrm{CII}],\mathrm{obs}}$ being the observed frequency of the [C II] line in GHz, and D_L the luminosity distance in Mpc.

To estimate the far-infrared luminosity, L_{FIR}, of the quasar host galaxies, we need to assume a function form of the dust spectral energy distribution (SED) and integrate the emission between the rest-frame wavelengths of 42.5 and 122.5 μm (e.g., Helou et al. 1988). Following the literature, we assume that the dust SED can be described by a modified blackbody with a dust temperature of $T_d = 47$ K and an emissivity index of $\beta = 1.6$ (e.g., Beelen et al. 2006; Leipski et al. 2014; Venemans et al. 2018). Under these assumptions, the FIR luminosity can be derived from the continuum flux density using the following equation:

$$L_{\mathrm{FIR}}/L_\odot = 3.86 \times 10^3\,\frac{S_{1900\,\mathrm{GHz}}}{f_{\mathrm{CMB}}(z)}\,\frac{D_L^2}{1+z}, \quad (3)$$

with f_{CMB} being the fraction of the continuum flux density measured against the cosmic microwave background (CMB; see da Cunha et al. 2013 for a detailed review of this effect), given by

$$f_{\mathrm{CMB}} = 1 - \frac{B_{\nu,[\mathrm{CII}],0}(T_{\mathrm{CMB}}(z)}{B_{\nu,[\mathrm{CII}],0}(T_d = 47\,K))}, \quad (4)$$

with $B_{\nu,[\mathrm{CII}],0}$ being the Planck function at the rest frequency of the [C II] line ($\nu_{[\mathrm{CII}],0} = 1900.54$ GHz), and $T_{\mathrm{CMB}}(z)$ the temperature of the CMB at redshift z. We here ignore the dust heating by the CMB, which has a negligible effect on the derived FIR luminosity (<1%) for our assumed dust temperature. The systematic uncertainty on the FIR luminosity due to the unknown shape of the dust SED is a factor of ∼2–3 (see Venemans et al. 2018 for an extended discussion).

Under the assumption that the dust is heated by star formation, we integrate the dust spectral energy distribution between the rest-frame wavelengths of 8 and 1000 μm (e.g., Kennicutt & Evans 2012) to obtain the total infrared luminosity L_{TIR} and convert L_{TIR} to an SFR. Adopting a modified blackbody with the canonical $T_d = 47$ K and $\beta = 1.6$ to describe the dust SED, we find the correspondence between L_{FIR} and L_{TIR} is $L_{\mathrm{TIR}} = 1.41 \times L_{\mathrm{FIR}}$. If we subsequently apply the local relation between L_{TIR} and SFR from Murphy et al. (2011),

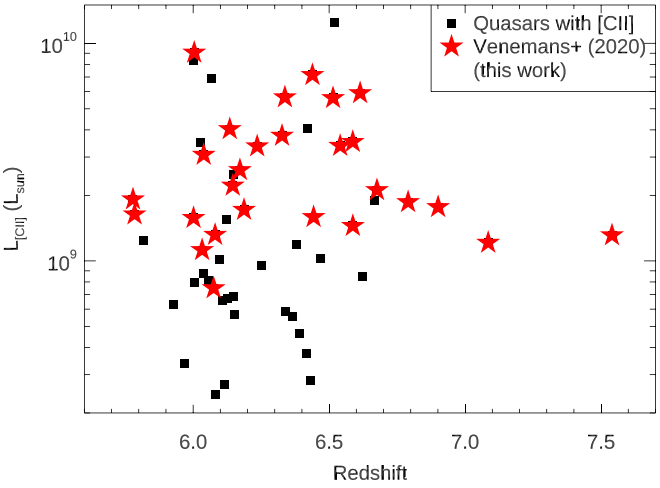

Figure 1. [C II] luminosity as a function of redshift for the quasars in our sample (red stars) and for all known $z > 5.7$ quasars from the literature (black squares). The observations presented here targeted the brighter quasar hosts known at these redshifts. Our sample contains 47% of all quasars at $z > 5.7$ with a [C II] detection and 68% of those with $L_{[\mathrm{CII}]} > 10^9\,L_\odot$.

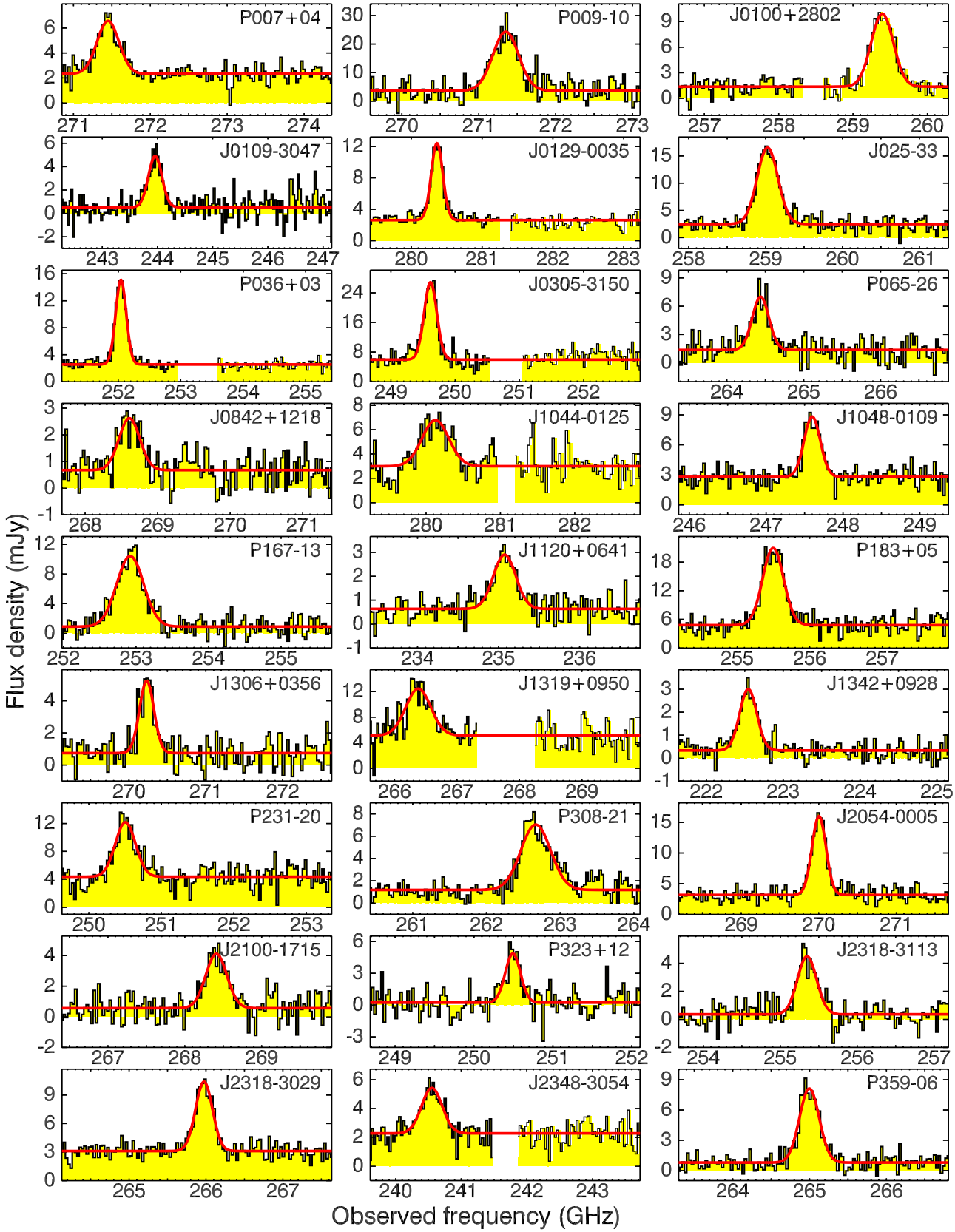

Figure 2. [C II] spectra of the 27 quasars in our sample, based on the two bandpasses encompassing the [C II] emission line. The spectra were extracted using aperture photometry with residual scaling (discussed in detail in Novak et al. 2019, 2020). The solid red line represents the Gaussian+continuum fit to the spectra (tabulated in Table 2).

Table 2
Results from Spectral Fitting of the Total [C II] Spectra Shown in Figure 2

Name	$z_{[CII]}$	$F_{[CII]}$ (Jy km s^{-1})	FWHM$_{[CII]}$ (km s^{-1})	$S_{1900\,GHz}$ (mJy)	EW$_{[CII]}$ (μm)	$L_{[CII]}$ ($10^9\,L_\odot$)	L_{FIR} ($10^{12}\,L_\odot$)	$L_{[CII]}/L_{FIR}$ (10^{-3})
P007+04	6.0015 ± 0.0002	1.67 ± 0.10	370 ± 22	2.33 ± 0.06	0.38 ± 0.02	1.58 ± 0.09	4.52 ± 0.11	0.35 ± 0.02
P009–10	6.0040 ± 0.0003	9.60 ± 0.70	437 ± 33	3.66 ± 0.36	1.38 ± 0.17	9.07 ± 0.66	7.13 ± 0.69	1.27 ± 0.15
J0100+2802	6.3269 ± 0.0002	3.69 ± 0.17	405 ± 20	1.37 ± 0.09	1.42 ± 0.11	3.76 ± 0.17	2.92 ± 0.18	1.29 ± 0.10
J0109–3047	6.7904 ± 0.0003	1.65 ± 0.14	354 ± 34	0.52 ± 0.08	1.67 ± 0.29	1.87 ± 0.16	1.26 ± 0.19	1.49 ± 0.26
J0129–0035	5.7788 ± 0.0001	2.15 ± 0.08	206 ± 9	2.61 ± 0.06	0.43 ± 0.02	1.92 ± 0.07	4.76 ± 0.11	0.40 ± 0.02
J025–33	6.3373 ± 0.0002	5.53 ± 0.21	370 ± 16	2.49 ± 0.11	1.17 ± 0.07	5.65 ± 0.22	5.31 ± 0.24	1.06 ± 0.06
P036+03	6.5405 ± 0.0001	3.16 ± 0.09	237 ± 7	2.55 ± 0.05	0.65 ± 0.02	3.38 ± 0.09	5.77 ± 0.12	0.59 ± 0.02
J0305–3150[a]	6.6139 ± 0.0002	5.43 ± 0.33	225 ± 15	5.34 ± 0.19	0.53 ± 0.04	5.90 ± 0.36	12.30 ± 0.44	0.48 ± 0.03
P065–26	6.1871 ± 0.0003	1.74 ± 0.17	289 ± 31	1.37 ± 0.11	0.67 ± 0.09	1.71 ± 0.17	2.80 ± 0.23	0.61 ± 0.08
J0842+1218	6.0754 ± 0.0005	0.78 ± 0.10	378 ± 52	0.68 ± 0.06	0.61 ± 0.09	0.75 ± 0.10	1.34 ± 0.11	0.56 ± 0.09
J1044–0125	5.7846 ± 0.0005	1.83 ± 0.23	454 ± 60	3.00 ± 0.12	0.32 ± 0.04	1.64 ± 0.21	5.48 ± 0.22	0.30 ± 0.04
J1048–0109	6.6759 ± 0.0002	1.92 ± 0.14	299 ± 24	2.79 ± 0.08	0.36 ± 0.03	2.11 ± 0.15	6.54 ± 0.19	0.32 ± 0.03
P167–13	6.5144 ± 0.0003	5.27 ± 0.25	519 ± 25	0.89 ± 0.12	3.11 ± 0.44	5.60 ± 0.27	2.00 ± 0.27	2.80 ± 0.40
J1120+0641	7.0848 ± 0.0004	1.01 ± 0.09	416 ± 39	0.64 ± 0.05	0.83 ± 0.10	1.21 ± 0.11	1.66 ± 0.12	0.73 ± 0.08
P183+05	6.4386 ± 0.0002	6.84 ± 0.31	397 ± 19	4.79 ± 0.16	0.75 ± 0.04	7.15 ± 0.32	10.53 ± 0.36	0.68 ± 0.04
J1306+0356	6.0330 ± 0.0002	1.18 ± 0.11	246 ± 26	0.74 ± 0.08	0.83 ± 0.12	1.12 ± 0.11	1.46 ± 0.16	0.77 ± 0.11
J1319+0950	6.1347 ± 0.0005	4.14 ± 0.43	532 ± 57	5.13 ± 0.22	0.42 ± 0.05	4.03 ± 0.42	10.36 ± 0.44	0.39 ± 0.04
J1342+0928	7.5400 ± 0.0003	1.00 ± 0.07	353 ± 27	0.34 ± 0.04	1.57 ± 0.20	1.32 ± 0.09	0.99 ± 0.10	1.34 ± 0.17
P231–20	6.5869 ± 0.0004	3.26 ± 0.28	393 ± 35	4.37 ± 0.15	0.39 ± 0.04	3.53 ± 0.30	9.99 ± 0.34	0.35 ± 0.03
P308–21	6.2355 ± 0.0003	3.37 ± 0.19	541 ± 32	1.18 ± 0.08	1.50 ± 0.13	3.37 ± 0.19	2.45 ± 0.16	1.37 ± 0.12
J2054–0005	6.0389 ± 0.0001	3.23 ± 0.14	236 ± 12	3.15 ± 0.10	0.54 ± 0.03	3.08 ± 0.14	6.20 ± 0.19	0.50 ± 0.03
J2100–1715	6.0807 ± 0.0004	1.37 ± 0.14	361 ± 41	0.56 ± 0.08	1.27 ± 0.22	1.31 ± 0.14	1.12 ± 0.16	1.17 ± 0.20
P323+12	6.5872 ± 0.0004	1.34 ± 0.17	271 ± 38	0.23 ± 0.12	3.04 ± 1.58	1.45 ± 0.19	0.53 ± 0.27	2.74 ± 1.42
J2318–3113	6.4429 ± 0.0003	1.52 ± 0.14	344 ± 34	0.36 ± 0.08	2.21 ± 0.50	1.59 ± 0.14	0.79 ± 0.17	2.00 ± 0.46
J2318–3029	6.1456 ± 0.0002	2.27 ± 0.12	293 ± 17	3.11 ± 0.07	0.38 ± 0.02	2.22 ± 0.12	6.29 ± 0.14	0.35 ± 0.02
J2348–3054	6.9007 ± 0.0005	1.53 ± 0.16	457 ± 49	2.28 ± 0.07	0.35 ± 0.04	1.77 ± 0.18	5.66 ± 0.18	0.31 ± 0.03
P359–06	6.1719 ± 0.0002	2.66 ± 0.13	341 ± 18	0.79 ± 0.07	1.78 ± 0.19	2.62 ± 0.13	1.60 ± 0.15	1.63 ± 0.17

Note.
[a] Values taken from Venemans et al. (2019).

we compute the SFR from L_{FIR} using

$$\mathrm{SFR}/M_\odot\ \mathrm{yr}^{-1} = 2.1 \times 10^{-10}\, L_{FIR}. \quad (5)$$

The [C II] luminosities of the quasar hosts in our sample range from $L_{[CII]} = 7.5 \times 10^8\,L_\odot$ to $L_{[CII]} = 9.1 \times 10^9\,L_\odot$, with a mean of $3.0 \times 10^9\,L_\odot$. This is slightly brighter than the average [C II] line luminosity of all $z \sim 6$ quasars studied so far ($2.4 \times 10^9\,L_\odot$; see Figure 1).

3.2. 2D Maps and Size Measurements

In Figure 3 we show the map of the continuum emission, the continuum-subtracted [C II] map (created by averaging over $1.2 \times$ FWHM$_{[CII]}$ around the redshifted [C II] line), and the EW$_{[CII]}$ map. The [C II]/FIR luminosity ratio will be discussed in Section 4.3.

We measured the extent of the sources in both the [C II] and continuum map by fitting a 2D Gaussian to the sources using the CASA task IMFIT. The results are listed in Table 3. All of the quasars are resolved in our [C II] maps, with deconvolved sizes ranging from $0\farcs18 \times 0\farcs10$ from the most compact quasar host galaxy to $0\farcs85 \times 0\farcs70$ for the most extended quasar host. In physical units, these sizes correspond to ~1.0–4.8 kpc. We stress that these size measurements only concern the bright, central emission and do not take extended low-surface-brightness emission into account. The extended emission will be described in an accompanying paper (Novak et al. 2020). In the continuum maps, three quasars (J0842+1218, J2100–1715, and P323+12) are not resolved as their measured sizes are consistent with the beam size.

The sizes of the [C II] and continuum emission are shown in Figure 4. As reported previously for quasar hosts (e.g., Wang et al. 2013; Willott et al. 2013; Venemans et al. 2016) and for high-redshift star-forming galaxies (e.g., Capak et al. 2015; Gullberg et al. 2018; Rybak et al. 2019, 2020), the continuum emission is more centrally concentrated than the [C II] emission. As already shown in Venemans et al. (2019) and further discussed in Novak et al. (2020), this does not mean that the [C II] emission is more extended than the continuum emission when considering faint emission: the size over which both [C II] and continuum emission can be traced is approximately equal (see Novak et al. 2020). The different radial profile of the line and continuum emission has an effect on the [C II]/FIR luminosity ratio, which we discuss in Section 4.3.

The quasar host galaxies have a range of different morphologies. Although some of the sources show regular morphologies, others clearly show substructure. Six of the quasars have already-published companion galaxies detected in [C II]. Most notably, Decarli et al. (2017) reported bright [C II]-emitting galaxies near four $z \sim 6$ quasars: J0842+1218 and J2100–1715 have a companion galaxy several arcseconds (up to 50 kpc) away from the quasar, while P231–20 has a more nearby companion galaxy and P308–21 is merging with a satellite galaxy (see also Decarli et al. 2019). Willott et al. (2017) reported a neighboring galaxy ~1″ away from quasar P167–13. This companion was confirmed by Neeleman et al. (2019) using higher-spatial-resolution observations. They also presented a new companion to J1306+0356. Venemans et al. (2019) reported

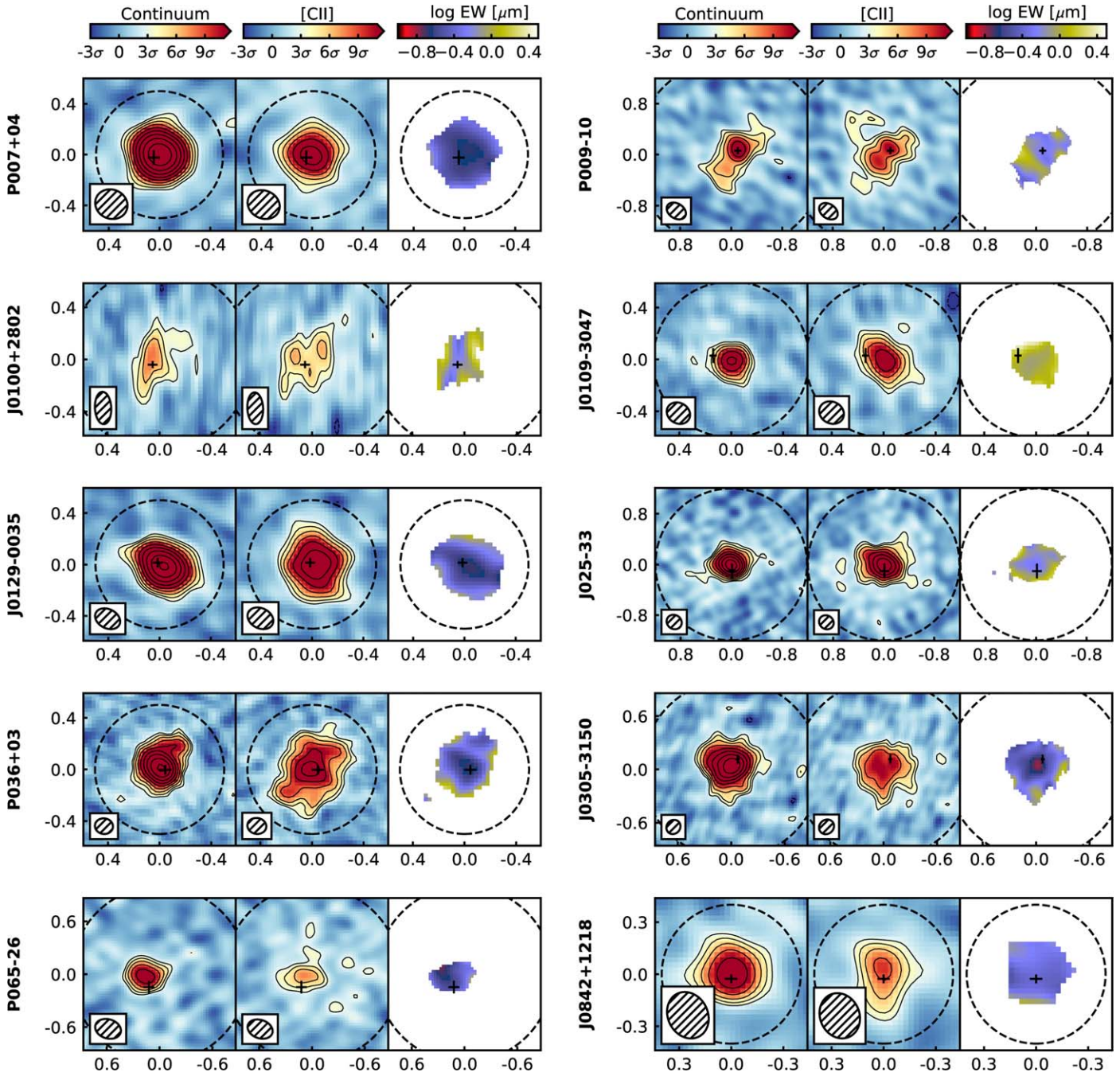

Figure 3. Maps of the continuum, [C II], and [C II] rest-frame equivalent width for the 27 quasars in our sample. The axes are in arcsec. The contours start at 3σ and increase in powers of $\sqrt{2}$. The cross indicates the position of the optical/near-infrared quasar (Table 1). The dashed line represents the aperture in which the total [C II] spectrum was extracted, as shown in Figure 2.

three [C II] emitters in the field of J0305–3150, of which two were within 1″ of the quasar. Besides P308–21, J1342+0942 also has a morphology consistent with undergoing a merger (Bañados et al. 2019).

We visually inspected all maps for nearby galaxies or disturbed [C II] morphologies. We also performed an automated search for companion galaxies in the field (see Section 3.3). From the maps, we identify a close companion to the quasar J1319+0950, which has not been reported before. Despite the fact that caution is warranted when identifying substructure in low- or even moderate-S/N interferometric data (e.g., Hodge et al. 2016), we found several sources, in particular P009–10, P065–26, and J2318–3113, that seem to have an irregular [C II] morphology (see also M. Neeleman et al. 2020, in preparation). This indicates that a significant fraction of the $z \sim 6$ quasar host galaxies are interacting with close companions or have disturbed morphologies.

3.3. Line Emitters in the Field

To identify potential new companion galaxies, we searched a total of 56 original (i.e., not continuum-subtracted) data cubes for galaxies with an emission line. The number of data cubes

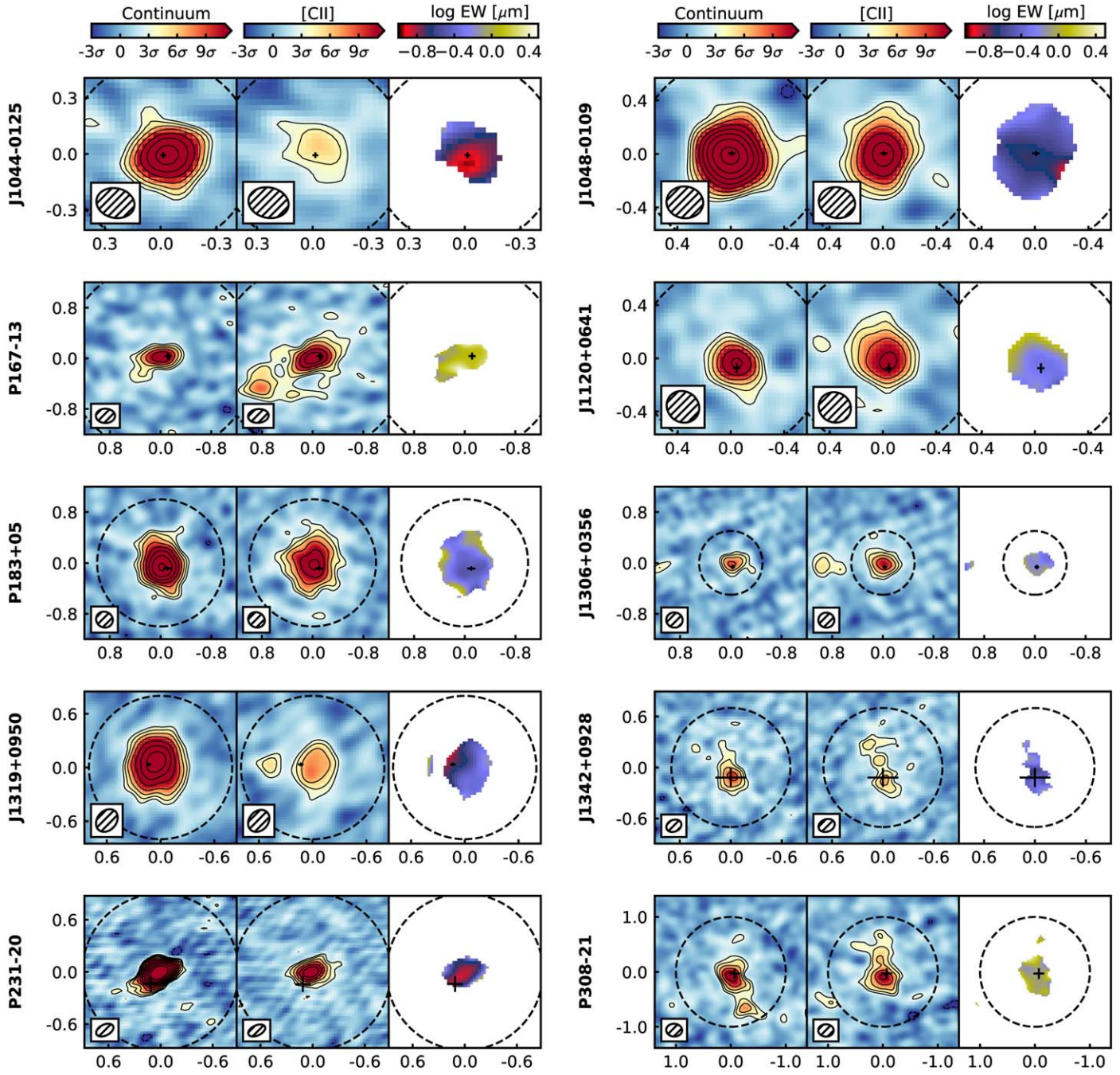

Figure 3. (Continued.)

was two to three per quasar field, one covering the two bandpasses around the redshifted [C II] emission line of the quasar and one or two covering the continuum bandpasses (see Section 2.2). We followed a procedure that is similar to that described in González-López et al. (2019) but with a few differences. We searched the cubes by channel for pixels reaching an S/N threshold of 3. To avoid including the same source multiple times, we remove candidates within 0.″5 and 1000 km s^{-1} of the highest-S/N candidates. To search for broader lines, we convolved the data cubes along the frequency axis with a Gaussian kernel with a standard deviation increasing incrementally by 30 MHz up to 400 MHz (approximately 500 km s^{-1}). We combined the results of each convolution and again removed sources within the distance and frequency thresholds (0.″5 and 1000 km s^{-1}, respectively) to avoid double counting the same line candidates.

To assign fidelity estimates to our list of candidates, we first repeated the line search process except we inverted the cube, searching for the brightest negative peaks at various line widths. For each line width, we binned the detected positive and negative candidates by S/N ratio and computed the fidelity:

$$f = 1 - \frac{n_{\mathrm{negative},i}}{n_{\mathrm{positive}},\, i}, \tag{6}$$

where $n_{\mathrm{negative},i}$ and $n_{\mathrm{positive},i}$ are the numbers of negative and positive candidates in an S/N bin i. For our search, we only considered candidates with a fidelity $\geqslant$0.8.

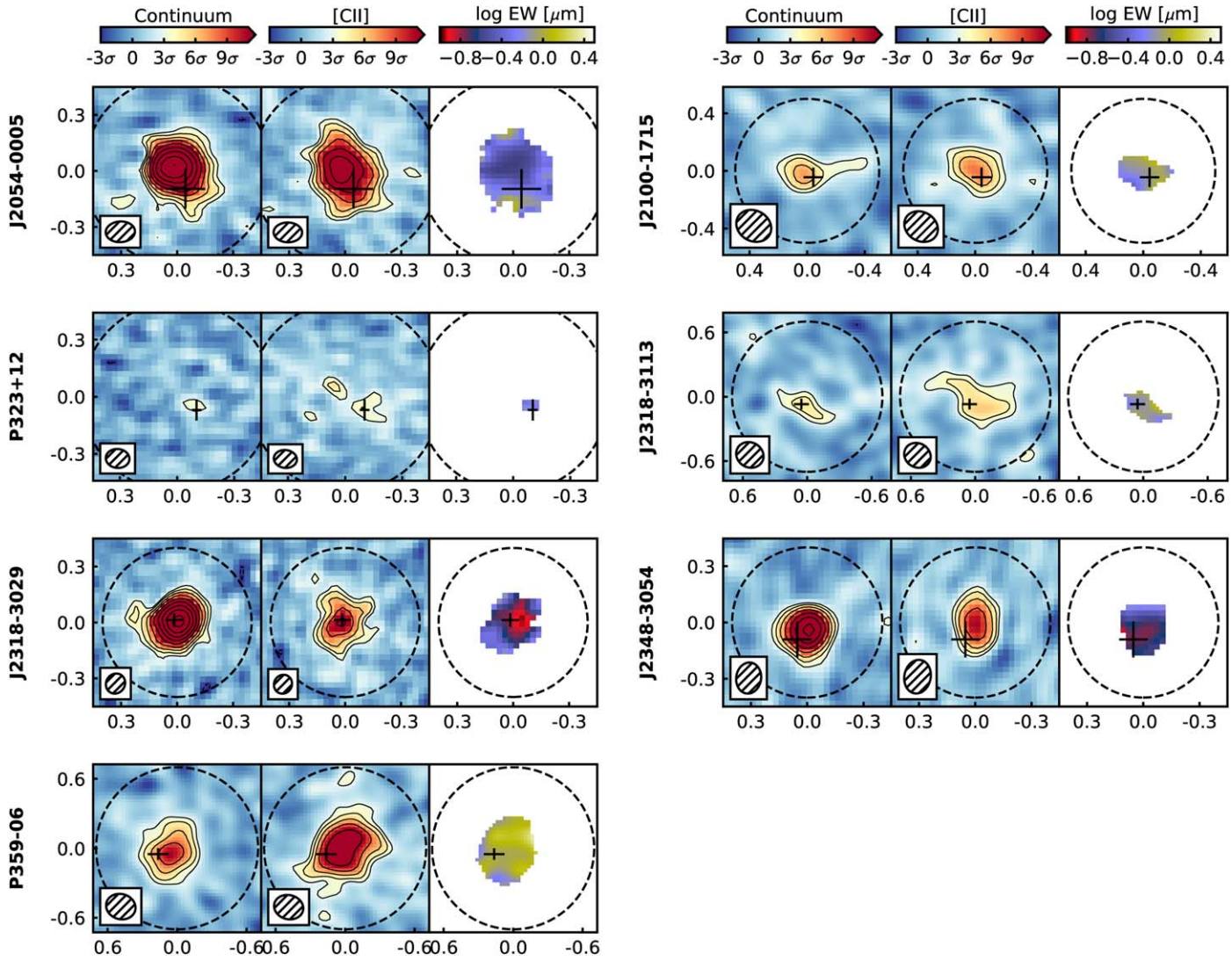

Figure 3. (Continued.)

The line search code yielded a total of 403 (305) candidate line emitters with a fidelity above 0.8 (0.9) in 56 data cubes. We visually inspected all candidates and discarded the ones that were dominated by continuum emission or extended line emission from the quasar (136 sources) or by imaging artifacts such as side lobes (54 sources). We fitted the spectra of the remaining 213 candidates with a Gaussian profile. We rejected 50 candidates with a line width of $\lesssim$50 km s^{-1} (i.e., a single channel of emission), as these are likely to be noise. We subsequently created channel maps both centered on and away from the line emission (see Appendix B for details) and removed 136 objects for which the imaging showed issues, such as the emission falling on top of severe striping. This left 27 candidate line emitters (of which 26 had fidelity >0.9).

We confirmed 10 previously detected emission line sources (Decarli et al. 2017; Willott et al. 2017; Neeleman et al. 2019; Venemans et al. 2019) and present 17 new candidate line emitters. The properties of all emission line candidates are listed in Table 4. We further discuss the candidates that are likely associated with the quasars in Section 4.4.

4. Discussion

4.1. Quasar Location

It is typically assumed that the supermassive black hole of a quasar host galaxy is located at the very center of the gravitational potential of a given dark matter halo. The gaseous component (that partly fuels the supermassive black hole) is also located toward this gravitational center. This is also seen in simulations, where the central regions of dark matter halos are those where the infalling gas accumulates. The exact position of the black hole is typically put in "by hand" at the bottom of the potential well in most simulations (e.g., Weinberger et al. 2017), although not all (e.g., Bartlett et al. 2020). It is therefore interesting to see if the gas (and dust) seen in the quasar hosts is indeed cospatial and centered on the supermassive black hole. With accurate quasar positions now available through matching to the Gaia DR2 catalog, leading to positional accuracies of <0.″15 (Section 2.3), and <0.″3 imaging of the [C II] line and dust continuum, we now have the measurements in hand to characterize any possible offsets between the gas and the

Table 3
[C II] and Continuum Size Measurements from IMFIT

Name	[C II] Size	[C II] Deconvolved Size	[C II] Dec. Size (kpc^2)	Cont. Size	Cont. Deconvolved Size	Cont. Dec. Size (kpc^2)
P007+04	$0\farcs33 \times 0\farcs32$	$0\farcs24 \times 0\farcs21$	1.4×1.2	$0\farcs28 \times 0\farcs26$	$0\farcs13 \times 0\farcs11$	0.7×0.6
P009–10	$0\farcs87 \times 0\farcs68$	$0\farcs84 \times 0\farcs60$	4.8×3.4	$0\farcs84 \times 0\farcs48$	$0\farcs80 \times 0\farcs35$	4.6×2.0
J0100+2802	$0\farcs54 \times 0\farcs42$	$0\farcs52 \times 0\farcs36$	2.9×2.0	$0\farcs51 \times 0\farcs30$	$0\farcs47 \times 0\farcs24$	2.6×1.3
J0109–3047	$0\farcs35 \times 0\farcs26$	$0\farcs29 \times 0\farcs19$	1.6×1.0	$0\farcs24 \times 0\farcs21$	$0\farcs15 \times 0\farcs13$	0.8×0.7
J0129–0035	$0\farcs37 \times 0\farcs33$	$0\farcs32 \times 0\farcs27$	1.9×1.6	$0\farcs29 \times 0\farcs22$	$0\farcs20 \times 0\farcs16$	1.2×1.0
J025–33	$0\farcs50 \times 0\farcs38$	$0\farcs44 \times 0\farcs32$	2.5×1.7	$0\farcs36 \times 0\farcs30$	$0\farcs27 \times 0\farcs19$	1.5×1.1
P036+03	$0\farcs45 \times 0\farcs32$	$0\farcs43 \times 0\farcs29$	2.4×1.6	$0\farcs23 \times 0\farcs21$	$0\farcs19 \times 0\farcs16$	1.0×0.8
J0305–3150	$0\farcs54 \times 0\farcs51$	$0\farcs52 \times 0\farcs48$	2.8×2.6	$0\farcs36 \times 0\farcs32$	$0\farcs32 \times 0\farcs28$	1.7×1.5
P065–26	$0\farcs90 \times 0\farcs73$	$0\farcs85 \times 0\farcs70$	4.8×3.9	$0\farcs36 \times 0\farcs29$	$0\farcs21 \times 0\farcs18$	1.2×1.0
J0842+1218	$0\farcs40 \times 0\farcs33$	$0\farcs32 \times 0\farcs20$	1.8×1.1	$0\farcs31 \times 0\farcs27$	$<0\farcs28 \times 0\farcs23$	$<1.6 \times 1.3$
J1044–0125	$0\farcs43 \times 0\farcs32$	$0\farcs37 \times 0\farcs27$	2.2×1.6	$0\farcs27 \times 0\farcs22$	$0\farcs18 \times 0\farcs14$	1.1×0.8
J1048–0109	$0\farcs43 \times 0\farcs36$	$0\farcs37 \times 0\farcs24$	2.0×1.3	$0\farcs33 \times 0\farcs33$	$0\farcs23 \times 0\farcs19$	1.2×1.0
P167–13	$0\farcs85 \times 0\farcs44$	$0\farcs79 \times 0\farcs37$	4.3×2.0	$0\farcs57 \times 0\farcs32$	$0\farcs48 \times 0\farcs22$	2.6×1.2
J1120+0641	$0\farcs41 \times 0\farcs38$	$0\farcs33 \times 0\farcs30$	1.7×1.5	$0\farcs33 \times 0\farcs26$	$0\farcs21 \times 0\farcs11$	1.1×0.6
P183+05	$0\farcs71 \times 0\farcs61$	$0\farcs66 \times 0\farcs55$	3.6×3.0	$0\farcs51 \times 0\farcs43$	$0\farcs45 \times 0\farcs35$	2.4×1.9
J1306+0356	$0\farcs49 \times 0\farcs38$	$0\farcs42 \times 0\farcs29$	2.4×1.7	$0\farcs38 \times 0\farcs30$	$0\farcs28 \times 0\farcs18$	1.6×1.0
J1319+0950	$0\farcs57 \times 0\farcs49$	$0\farcs52 \times 0\farcs41$	3.0×2.3	$0\farcs47 \times 0\farcs41$	$0\farcs39 \times 0\farcs33$	2.2×1.8
J1342+0928	$0\farcs81 \times 0\farcs45$	$0\farcs80 \times 0\farcs40$	4.0×2.0	$0\farcs53 \times 0\farcs31$	$0\farcs51 \times 0\farcs25$	2.5×1.2
P231–20	$0\farcs31 \times 0\farcs20$	$0\farcs24 \times 0\farcs16$	1.3×0.8	$0\farcs24 \times 0\farcs15$	$0\farcs11 \times 0\farcs09$	0.6×0.5
P308–21	$0\farcs77 \times 0\farcs52$	$0\farcs73 \times 0\farcs44$	4.1×2.4	$0\farcs99 \times 0\farcs44$	$0\farcs96 \times 0\farcs34$	5.4×1.9
J2054–0005	$0\farcs32 \times 0\farcs24$	$0\farcs29 \times 0\farcs19$	1.7×1.1	$0\farcs20 \times 0\farcs19$	$0\farcs16 \times 0\farcs13$	0.9×0.7
J2100–1715	$0\farcs43 \times 0\farcs33$	$0\farcs36 \times 0\farcs25$	2.0×1.4	$0\farcs45 \times 0\farcs21$	$<0\farcs25 \times 0\farcs21$	$<1.4 \times 1.2$
P323+12	$0\farcs61 \times 0\farcs26$	$0\farcs59 \times 0\farcs24$	3.2×1.3	$0\farcs15 \times 0\farcs10$	$<0\farcs12 \times 0\farcs10$	$<0.7 \times 0.5$
J2318–3113	$0\farcs91 \times 0\farcs48$	$0\farcs87 \times 0\farcs42$	4.8×2.3	$1\farcs04 \times 0\farcs33$	$1\farcs00 \times 0\farcs22$	5.5×1.2
J2318–3029	$0\farcs27 \times 0\farcs22$	$0\farcs25 \times 0\farcs20$	1.4×1.1	$0\farcs18 \times 0\farcs15$	$0\farcs14 \times 0\farcs12$	0.8×0.7
J2348–3054	$0\farcs26 \times 0\farcs18$	$0\farcs18 \times 0\farcs10$	1.0×0.5	$0\farcs19 \times 0\farcs18$	$0\farcs13 \times 0\farcs07$	0.7×0.4
P359–06	$0\farcs52 \times 0\farcs39$	$0\farcs47 \times 0\farcs30$	2.6×1.7	$0\farcs45 \times 0\farcs38$	$0\farcs40 \times 0\farcs28$	2.2×1.6

central black hole. Any offset in position could be due to a number of things, such as infalling gas that has not fully settled in a disk, the presence of mergers that shift the center of mass in the quasar host, or the possibility that the supermassive black hole is in fact not located at the precise center of the potential well.

The locations of the accreting black holes are listed in Table 1, and the central positions and uncertainty of the dust continuum and [C II] emission are the centroid position obtained by IMFIT. The results are shown in Figure 5. For most sources, the center of the dust emission coincides with the optical/near-infrared point source to within $0\farcs1$. Although in most cases not significant, the predominantly positive offset in decl. could be due to differential chromatic refraction when calculating the optical positions (see Section 2.3), but the effect seems to be much smaller than the typical beam of $0\farcs25$ of our ALMA observations. As gas traced by the [C II] emission extends to large radii in the quasar hosts, we also compared the position of the quasars with the [C II] position (the centroid provided by IMFIT) in Figure 5. Although the offsets are on average slightly larger, still the majority of sources do not show a significant offset. Several sources with known nearby companions, P231–20, P167–13, J0305–3150, and P308–21, show offsets between the quasar and the dust emission in the host galaxy. Intriguingly, two sources without known companions, P065–26 and J0109–3047, show significant offsets between the optical position of the central quasar and that of both the dust and [C II] emission. For J0109–3047, a large velocity offset of $\sim$1700 km s^{-1} between the [C II] redshift and that of the broad emission lines near the black hole was reported (e.g., Venemans et al. 2016), which, combined with the spatial offsets presented here, could indicate that the quasar host galaxy has recently undergone an interaction with a different system. Alternatively, these offsets could be due to an outflow. Higher-spatial-resolution observations are required to

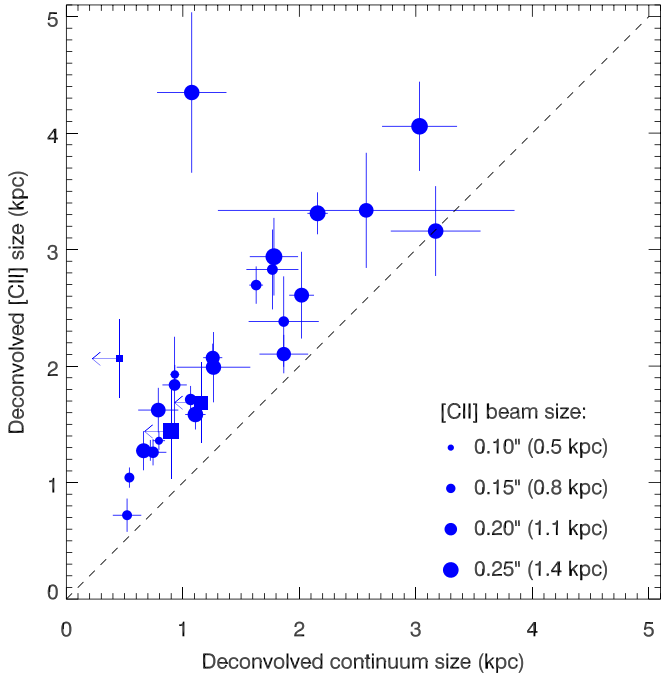

Figure 4. Width in kpc of the 2D Gaussian fit to the quasar host galaxies in the continuum (x-axis) and [C II] maps (y-axis). The sizes are deconvolved with the beam. The size of the symbols scales with the beam of the observations (listed in Table 1). Quasar hosts unresolved in the continuum image are indicated with a square and an arrow. The dashed line represents the 1:1 line. In general, the continuum emission is more centrally concentrated than the [C II] emission.

Table 4
Properties of Candidate Line Emitters Found in the Quasar Fields

Name	R.A. (ICRS)	Decl. (ICRS)	$\nu_{\rm center}$ (GHz)	F (Jy km s^{-1})	FWHM (km s^{-1})	$S_{\rm cont}$ (mJy)	S/N	Fidelity
J0100+2802C1	$01^{\rm h}00^{\rm m}14\overset{\rm s}{.}04$	$+28°02'17\overset{''}{.}4$	259.49 ± 0.03	0.80 ± 0.13	435 ± 78	<0.19	5.9	0.91
P036+03C1	$02^{\rm h}26^{\rm m}00\overset{\rm s}{.}80$	$+03°03'02\overset{''}{.}4$	254.78 ± 0.01	0.37 ± 0.07	103 ± 23	<0.19	5.9	1.00
P036+03C2	$02^{\rm h}26^{\rm m}01\overset{\rm s}{.}74$	$+03°02'53\overset{''}{.}5$	268.79 ± 0.01	0.04 ± 0.01	114 ± 28	<0.03	5.5	0.85
J0305–3150C1[a]	$03^{\rm h}05^{\rm m}16\overset{\rm s}{.}39$	$-31°50'55\overset{''}{.}0$	249.82 ± 0.04	1.14 ± 0.29	489 ± 132	0.66 ± 0.13	6.0	0.96
J0305–3150C2[a]	$03^{\rm h}05^{\rm m}16\overset{\rm s}{.}87$	$-31°50'55\overset{''}{.}3$	249.73 ± 0.01	0.21 ± 0.03	121 ± 22	0.16 ± 0.03	7.2	1.00
J0305–3150C3[a]	$03^{\rm h}05^{\rm m}16\overset{\rm s}{.}96$	$-31°50'55\overset{''}{.}8$	249.42 ± 0.03	0.66 ± 0.09	559 ± 80	0.54 ± 0.04	9.3	1.00
J0305–3150C4	$03^{\rm h}05^{\rm m}17\overset{\rm s}{.}19$	$-31°50'50\overset{''}{.}8$	252.30 ± 0.04	0.13 ± 0.06	207 ± 103	0.46 ± 0.04	5.9	0.94
J0842+1218C1[b]	$08^{\rm h}42^{\rm m}28\overset{\rm s}{.}97$	$+12°18'55\overset{''}{.}0$	269.00 ± 0.01	1.81 ± 0.13	331 ± 26	<0.22	18.9	1.00
J0842+1218C2[c]	$08^{\rm h}42^{\rm m}29\overset{\rm s}{.}67$	$+12°18'46\overset{''}{.}3$	269.04 ± 0.02	0.43 ± 0.09	268 ± 62	<0.17	7.5	1.00
J1044–0125C1	$10^{\rm h}44^{\rm m}32\overset{\rm s}{.}86$	$-01°24'51\overset{''}{.}9$	294.19 ± 0.01	0.30 ± 0.06	143 ± 34	<0.17	5.7	1.00
P167–13C1[d]	$11^{\rm h}10^{\rm m}34\overset{\rm s}{.}04$	$-13°29'46\overset{''}{.}3$	253.02 ± 0.01	1.26 ± 0.08	445 ± 30	0.17 ± 0.04	18.8	1.00
P183+05C1	$12^{\rm h}12^{\rm m}26\overset{\rm s}{.}32$	$+05°05'29\overset{''}{.}6$	255.61 ± 0.04	0.41 ± 0.12	373 ± 121	0.37 ± 0.06	5.7	0.92
P183+05C2	$12^{\rm h}12^{\rm m}28\overset{\rm s}{.}07$	$+05°05'34\overset{''}{.}6$	240.75 ± 0.01	0.27 ± 0.06	155 ± 35	<0.13	5.8	1.00
J1306+0356C1[c]	$13^{\rm h}06^{\rm m}08\overset{\rm s}{.}33$	$+03°56'26\overset{''}{.}2$	270.19 ± 0.01	1.29 ± 0.15	200 ± 26	0.35 ± 0.12	11.3	1.00
J1319+0950C1	$13^{\rm h}19^{\rm m}11\overset{\rm s}{.}65$	$+09°50'38\overset{''}{.}2$	269.50 ± 0.05	0.91 ± 0.22	490 ± 127	<0.28	5.9	0.95
J1319+0950C2	$13^{\rm h}19^{\rm m}11\overset{\rm s}{.}87$	$+09°50'44\overset{''}{.}3$	266.02 ± 0.02	0.35 ± 0.08	218 ± 55	0.19 ± 0.05	5.6	0.90
J1342+0928C1	$13^{\rm h}42^{\rm m}08\overset{\rm s}{.}24$	$+09°28'43\overset{''}{.}4$	222.70 ± 0.02	0.10 ± 0.03	222 ± 75	<0.06	5.8	1.00
J1342+0928C2	$13^{\rm h}42^{\rm m}08\overset{\rm s}{.}65$	$+09°28'44\overset{''}{.}2$	238.84 ± 0.04	0.69 ± 0.16	475 ± 117	1.76 ± 0.07	24.3	1.00
P231–20C1	$15^{\rm h}26^{\rm m}37\overset{\rm s}{.}11$	$-20°49'59\overset{''}{.}4$	251.86 ± 0.01	0.19 ± 0.04	145 ± 38	<0.11	6.0	0.96
P231–20C2	$15^{\rm h}26^{\rm m}37\overset{\rm s}{.}62$	$-20°49'58\overset{''}{.}6$	235.04 ± 0.01	0.12 ± 0.02	209 ± 45	<0.05	6.2	1.00
P231–20C3[b]	$15^{\rm h}26^{\rm m}37\overset{\rm s}{.}87$	$-20°50'02\overset{''}{.}3$	250.38 ± 0.01	2.81 ± 0.22	497 ± 41	1.52 ± 0.10	34.0	1.00
P231–20C4[c]	$15^{\rm h}26^{\rm m}37\overset{\rm s}{.}97$	$-20°50'02\overset{''}{.}5$	250.38 ± 0.03	0.25 ± 0.05	334 ± 77	0.10 ± 0.03	6.1	1.00
J2054–0005C1	$20^{\rm h}54^{\rm m}07\overset{\rm s}{.}01$	$-00°05'25\overset{''}{.}7$	270.03 ± 0.01	0.55 ± 0.15	106 ± 32	<0.46	5.8	0.92
J2100–1715C1[b]	$21^{\rm h}00^{\rm m}55\overset{\rm s}{.}45$	$-17°15'22\overset{''}{.}1$	268.42 ± 0.03	8.09 ± 1.07	600 ± 80	3.66 ± 0.46	15.4	1.00
J2318–3113C1	$23^{\rm h}18^{\rm m}18\overset{\rm s}{.}72$	$-31°13'49\overset{''}{.}9$	256.50 ± 0.01	0.09 ± 0.02	102 ± 26	<0.06	5.7	1.00
J2318–3113C2	$23^{\rm h}18^{\rm m}19\overset{\rm s}{.}36$	$-31°13'48\overset{''}{.}9$	254.85 ± 0.01	0.17 ± 0.05	111 ± 35	<0.13	5.6	0.99
J2318–3029C1	$23^{\rm h}18^{\rm m}33\overset{\rm s}{.}36$	$-30°29'44\overset{''}{.}5$	266.84 ± 0.04	0.93 ± 0.21	427 ± 104	<0.33	6.0	0.91

Notes.
[a] Previously known companion, published in Venemans et al. (2019).
[b] Previously known companion, published in Decarli et al. (2017).
[c] Previously known companion, published in Neeleman et al. (2019).
[d] Previously known companion, published in Willott et al. (2017).

distinguish between these two scenarios. The offsets measured for P065–26 could be, in part, due to systemic astrometric uncertainties as this source has been observed at high air mass. However, when comparing the position of the dust and the [C II] emission (Figure 6), P065–26 has the largest offset, together with the known merging system P308–21. Also, the [C II] emission of P065–26 appears to have an irregular, disturbed morphology (Figure 3).

We conclude that there is overall excellent agreement between the location of the supermassive black hole and the ISM of the quasar host, seen in both [C II] and dust continuum emission. In most cases, the offset is less than a few hundred parsecs, but some outliers with offsets of ∼750 pc exist. Those outliers can in many cases be linked to host galaxies that undergo interactions, which may lead to a displacement of the ISM due to gravitational interactions. For some sources, we cannot discard that the offsets are caused by outflows. The presence of outflows in our sample has been extensively discussed in Novak et al. (2020). Overall we conclude that, to first order, the center of mass of the ISM is cospatial (within the observational uncertainties of a few 100 pc) with the central supermassive black hole.

4.2. Star Formation Rate Density

An important question arising in FIR studies of high-redshift quasar host galaxies is the heating source of the dust. Models suggest that the high luminosity of the central quasar could potentially power a significant fraction of the dust emission for even the most FIR-luminous quasars (e.g., Schneider et al. 2015). Recently, Venemans et al. (2018) compared the quasar's bolometric luminosity and FIR luminosity of a large sample of $z > 5.7$ quasars and found only a weak correlation. However, the FIR luminosities used in Venemans et al. (2018) were mostly derived from unresolved observations. Therefore, it remains possible that the quasar still contributes significantly to the dust heating close to the accreting black hole. With the kiloparsec-resolution observations presented in this paper, we test whether this is the case for our sample of quasars. We measured the peak flux density in our continuum maps (Figure 3) and converted these values to FIR luminosities using Equation (3). The peak FIR surface densities are between 10^{11} and $10^{13}\,L_\odot\,{\rm kpc}^{-2}$. The bolometric luminosity $L_{\rm bol}$ of the quasars was taken from the literature (Table 3 in Venemans et al. 2018). In short, the quasar's bolometric luminosity is computed based on the rest-frame UV emission of the accreting black hole. We note that the quasars studied here are unobscured (Type I) quasars and show no signs of dust absorption in their UV spectra. We compared $L_{\rm bol}$ to the peak FIR surface density in Figure 7. The brightness of the central dust emission seems to be independent of the luminosity of the central active galactic nucleus (the Pearson correlation coefficient is $r = -0.04$). This suggests that even in the central kiloparsec of the hosts of luminous $z \sim 6$ quasars, the

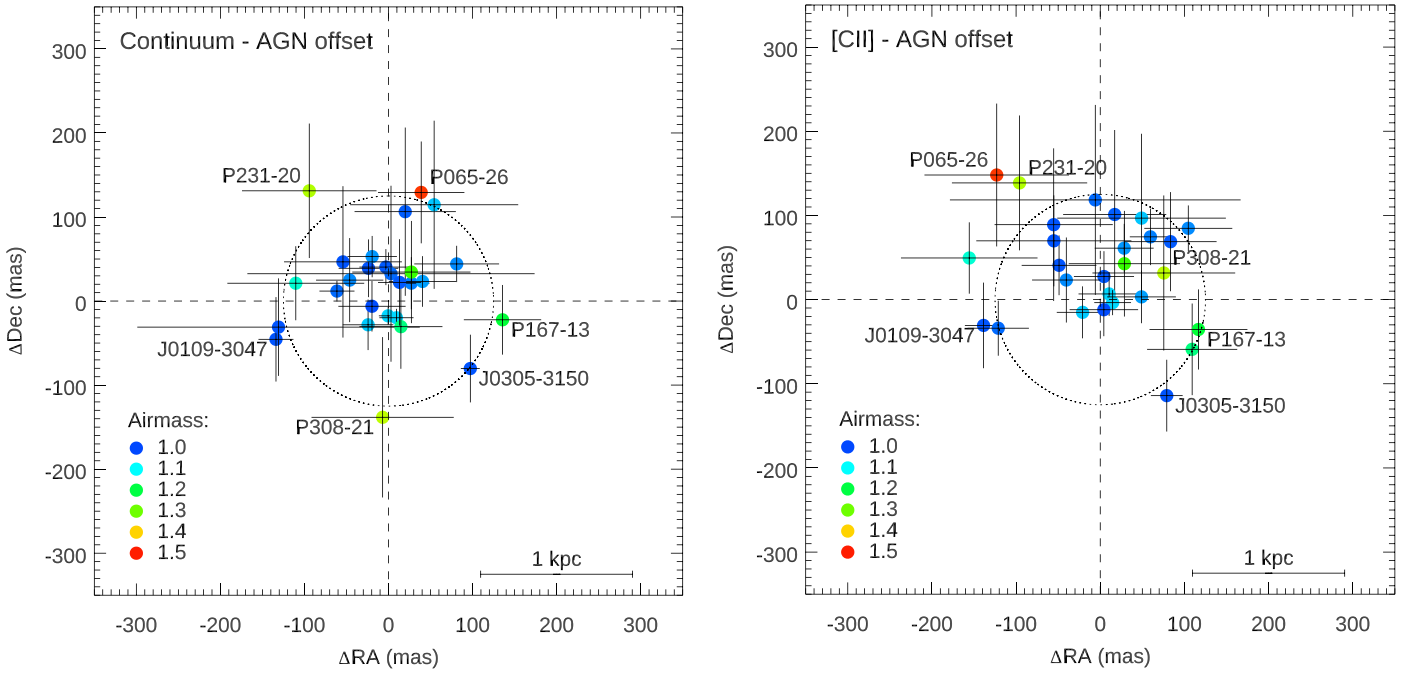

Figure 5. Left: difference in position on the sky between the accreting black hole (the quasar position) and the center of the 2D Gaussian fit to the continuum emission as reported by the CASA task IMFIT. The dotted circle represents the size of a typical, 0.″25 beam. The colors of the points indicate the minimum air mass of the optical/near-infrared imaging of the quasar. Objects with a significant ($>2\sigma$) offset are labeled. The known merger P308–21 is labeled as well. Right: same as the plot on the left, but here with the central position of the [C II] emission instead of the dust continuum.

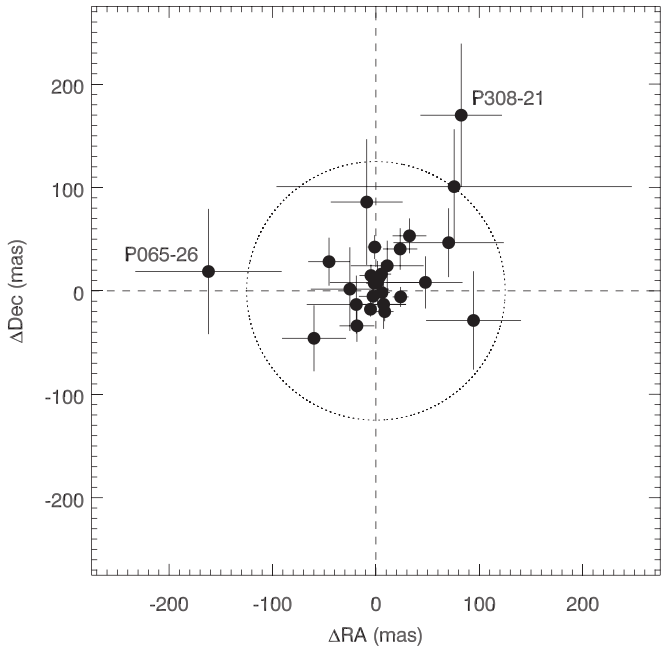

Figure 6. Offset between the center of the dust and that of the [C II] emission. For most of the quasar host galaxies in our sample, there are no significant offsets.

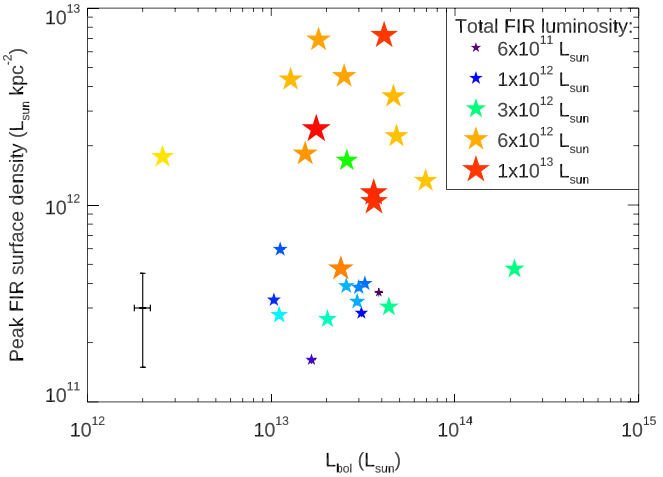

Figure 7. Peak FIR surface density vs. bolometric luminosity. The peak FIR luminosities were derived from the peak pixel in the continuum maps (Figure 3). The color of each point represents the total FIR luminosity of the quasar host as listed in Table 2. A typical error bar is shown in the lower left corner. There is no correlation between the brightness of the accreting black hole and the dust continuum peak flux density.

dust is predominantly heated by star formation. This is somewhat surprising, given that the accreting black hole, with a bolometric luminosity often a factor of 10 higher than the FIR luminosity, is sitting at the center of a dusty galaxy. The lack of heating by the AGN could be explained if the emission from the quasar is highly collimated and emitted perpendicular to the disk of the host galaxy. Alternatively, the obscuration of the central black hole could be anisotropic. With a large fraction of quasar host galaxies having a very close companion or undergoing a merger event (Section 3.2), the distribution of dust in the centers of the quasar hosts could show significant variation between sources, which in turn could erase any correlation between the emission of the accreting black hole and that of the surrounding dust.

In Figure 8 we show the SFR surface density (SFRD) in annuli around the center of the quasar host galaxy (defined as the peak of the dust continuum emission), derived from Equations (3) and (5). The peak SFRD spans a large range of nearly a factor of 50, from $30\,M_{\odot}\,\mathrm{yr}^{-1}\,\mathrm{kpc}^{-2}$ to $1500\,M_{\odot}\,\mathrm{yr}^{-1}\,\mathrm{kpc}^{-2}$. This range is larger than that of the total FIR luminosities covered by our sample (spanning a factor

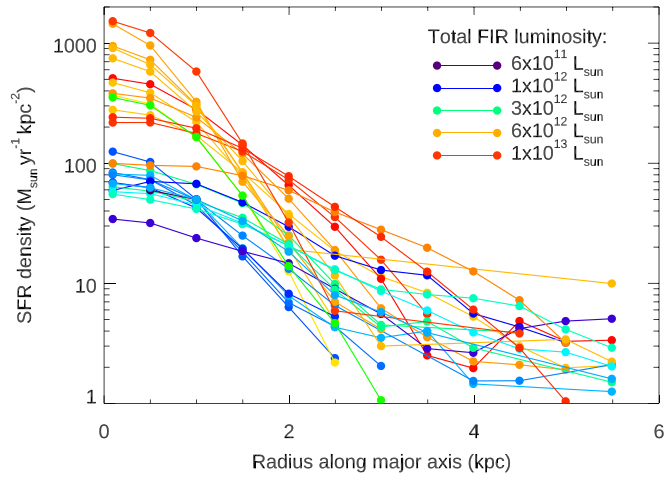

Figure 8. SFR surface density in the quasar host galaxies as a function of radius from the center. The SFR was derived from the dust continuum flux density (see text for details). Each quasar host galaxy is represented by a colored track with the color representing the total FIR luminosity of the source (Table 2). Most peak star formation rate densities are below the Eddington limit for star formation (i.e., $\lesssim$1000 $M_\odot$ yr^{-1} kpc^{-2}).

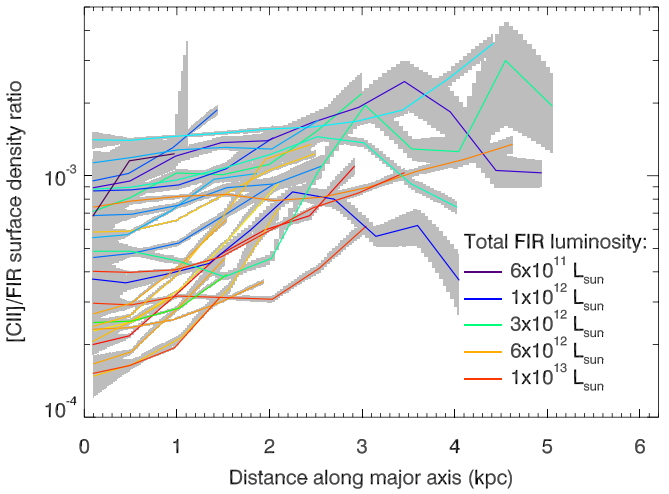

Figure 9. [C II]-to-FIR surface density luminosity ratio of our quasar sample as a function of distance from the center. The colors encode the total FIR luminosity of the sources (Table 2), and the gray regions represent the 1σ uncertainties in the luminosity ratio. On average, the [C II]/FIR ratio is lowest in the center of the galaxies.

of ∼25; see Table 2). While the highest SFRDs that we find approach that of the Eddington limit for star formation (e.g., Walter et al. 2009), as also seen in the centers of local ultraluminous infrared galaxies (ULIRGs; e.g., Downes & Solomon 1998) or Galactic star-forming regions such as Orion, most quasar host galaxies have central SFRD values well below such an extreme value (i.e., $\lesssim$1000 $M_\odot$ yr^{-1} kpc^{-2}). In the outskirts, SFRD values reach a few $M_\odot$ yr^{-1} kpc^{-2}, which is still significantly higher than typical star formation rate densities in nearby disk galaxies (i.e., $<$1 $M_\odot$ yr^{-1} kpc^{-2}, Leroy et al. 2013).

4.3. [C II]-to-FIR Ratio and [C II] Deficit

Studies of local ULIRGs show that their centers often display a low [C II]/FIR luminosity ratio, which is attributed to intense radiation fields in the nucleus (e.g., Smith et al. 2017; Herrera-Camus et al. 2018). In Figure 9 we show that generally the [C II]-to-FIR luminosity ratio is lower in the center of the quasar hosts, although the central values vary up to a factor of ∼10 within our sample. In the centers, we find surface density values as low as a few $\times 10^{-4}$, consistent with studies of $z > 1$ starburst galaxies (e.g., Lamarche et al. 2018; Litke et al. 2019; Rybak et al. 2020). Away from the central regions, at radii $>$2 kpc, the $L_{[\rm CII]}/L_{\rm FIR}$ ratio approaches luminosity ratios of $\sim 10^{-3}$, similar to what is found in the disks of local starburst galaxies (e.g., Díaz-Santos et al. 2013; Sargsyan et al. 2014).

To investigate the importance of the FIR surface density (i.e., the local radiation field) in driving the low [C II]/FIR luminosity ratios, we plot the $L_{[\rm CII]}/L_{\rm FIR}$ surface densities as a function of the FIR surface density $\Sigma_{\rm FIR}$ in Figure 10. We find that the lowest $L_{[\rm CII]}/L_{\rm FIR}$ ratios come from the regions that show the highest $L_{\rm FIR}$ values, that is, in the centers. This indicates that the intense radiation field in the centers of the quasar host galaxies (not necessarily due to the radiation of the accreting black hole; see Section 4.2) could be the cause of the [C II] deficit, similar to the results found for local starburst galaxies and quasars (e.g., Lutz et al. 2016; Smith et al. 2017; Herrera-Camus et al. 2018).

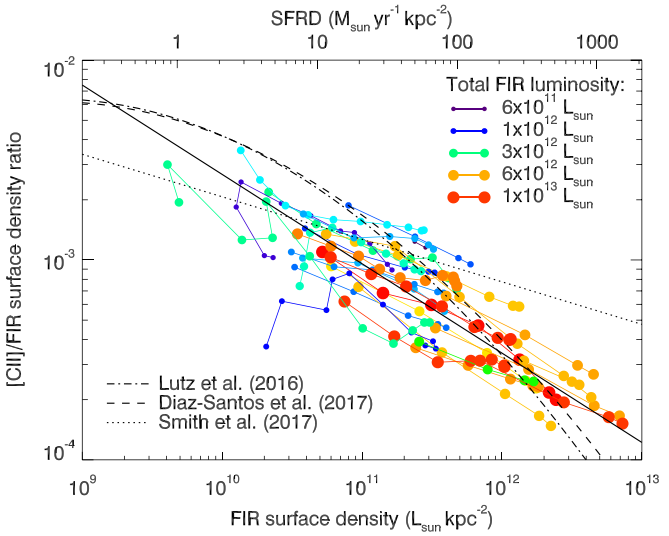

Figure 10. [C II]/FIR surface density luminosity ratio, now shown as a function of FIR luminosity density. The colors of the tracks again indicate the total FIR luminosity of the objects. Overplotted are relations between the [C II]/FIR surface densities and the FIR surface density from the literature, after converting their measurements to the assumptions and units used in this work (see legend for details). Our best-fit power-law fit to the data points is shown as a solid line.

We fitted a power law to the data in Figure 10 and found the following relation:

$$\Sigma_{\rm [CII]/FIR} = 9.6 \times 10^{-4} \left(\frac{\Sigma_{\rm FIR}}{10^{11} L_\odot \ {\rm kpc}^{-2}} \right)^{-0.447}. \quad (7)$$

The slope of this correlation is very similar to the one published by Díaz-Santos et al. (2014), who found a slope of -0.39 ± 0.07 for the extended regions in spatially resolved local (ultra)luminous infrared galaxies. This slope is significantly shallower than predicted by models, possibly caused in part by the reduced gas heating efficiency due to the ionization

of dust particles (see Díaz-Santos et al. 2014 for an extensive discussion). Our data in Figure 10 are below the relation presented by Smith et al. (2017). However, the data fitted by these authors were regions inside nearby galaxies, where FIR surface densities are a few orders of magnitude lower than those studied here. Both Lutz et al. (2016) and Díaz-Santos et al. (2017) also presented $L_{[CII]}/L_{FIR}$ ratios as a function of FIR surface density. Generally, they find a steeper relation with higher ratios at low FIR surface densities compared to our $z \sim 6$ quasar host galaxy sample, whereas at the highest densities, their fits predict lower values than reported here. These discrepancies could be due to our assumption of a single dust temperature everywhere in the quasar host galaxies, whereas studies of local galaxies (e.g., Díaz-Santos et al. 2017) report a range of dust temperatures. Furthermore, it has been shown in local galaxies that there is a relation between the infrared surface brightness and the dust temperature (e.g., Chanial et al. 2007). We note that the estimation of Σ_{FIR} is sensitive to the temperature that is used in the derivation of the luminosity. If the outskirts of our quasar hosts have lower dust temperatures compared to the centers, then our [C II]/FIR luminosity ratio would increase at low FIR surface densities. In particular, if the outskirts of the quasar host galaxies where $\Sigma_{FIR} \approx 2 \times 10^{10}\ L_{\odot}\,\mathrm{kpc}^{-2}$ have a lower dust temperature of $T_d = 35$ K (well within the range of dust temperatures spanned by local starburst galaxies; e.g., Díaz-Santos et al. 2017), then Σ_{FIR} will be a factor of ~2 lower, while $\Sigma_{[CII]/FIR}$ would be higher by this factor. This would place the outskirt of our quasar hosts on the local relations as found by Lutz et al. (2016) and Díaz-Santos et al. (2017). Similarly, if the centers of the quasar hosts are hotter, the [C II]-to-FIR ratio would decrease for the highest FIR surface densities. Future observations of the quasar hosts with ALMA band 8 or band 9 will shed light on this question.

4.4. Galaxy Clustering around High-redshift Quasars

In Section 3.3 we presented 27 candidate line emitters found in the fields of the 27 quasars in our sample. Ten of those were previously identified and published companion [C II]-emitting galaxies to the quasars (see Decarli et al. 2017; Willott et al. 2017; Neeleman et al. 2019; Venemans et al. 2019) with physical distances up to ~60 kpc and line-of-sight velocities $\Delta v < 600\ \mathrm{km\,s^{-1}}$. We note that we did not recover the known companion next to P308–21 (Decarli et al. 2017, 2019), because the quasar host galaxy is actively undergoing a merger and has very extended [C II] emission (see also Table 3). For the remaining 17 line candidates, we cannot determine a priori if they are [C II] emitters and whether they are associated with the quasar. For each line, we computed the redshift if the line was [C II] and calculated the line-of-sight velocity to the quasar. In the literature, velocity differences between $1000\ \mathrm{km\,s^{-1}}$ and $3000\ \mathrm{km\,s^{-1}}$ are typically used to identify sources that are associated with active galactic nuclei (e.g., Hennawi et al. 2006; Venemans 2006; Venemans et al. 2007; Ellison et al. 2010). We therefore conservatively assume that sources with a velocity difference of $\Delta v < 2000\ \mathrm{km\,s^{-1}}$ are associated with the quasar. Of the 27 emission line candidates, 19 (including the 10 known companions) are [C II]-emitting companion galaxies to the quasars, with 17 of those within $1000\ \mathrm{km\,s^{-1}}$ of the quasar. We list the nine new companion galaxies with derived line and continuum properties in Table 5, and we show the spectra and emission maps in Figure 11.

The next question is whether these companion sources represent an overdensity of galaxies around these high-redshift quasars. Spatially, there is no significant difference between the new companion galaxies and the other candidate line emitters, especially if the already-known, nearby (<10 kpc) companions are excluded. The fraction of all channels in our 56 data cubes that probe [C II] with a velocity difference of $<2000\ \mathrm{km\,s^{-1}}$ with respect to the quasar redshift is 38%. For $\Delta v < 1000\ \mathrm{km\,s^{-1}}$, this fraction is 22%. Based on the "field" density of line emitters (eight emission line candidates that have $\Delta v > 2000\ \mathrm{km\,s^{-1}}$), we would only expect ~5 (~3) emission line candidates with $\Delta v < 2000\ \mathrm{km\,s^{-1}}$ ($\Delta v < 1000\ \mathrm{km\,s^{-1}}$), where we find 19 (17).

This suggests that the emission line candidates are highly clustered around the redshift of the quasar, implying that the majority of sources within $2000\ \mathrm{km\,s^{-1}}$ are likely companion galaxies at similar redshifts. Assuming that all candidate line emitters are high-redshift [C II]-emitting galaxies, we calculated the average overdensity of quasar companions using

$$\delta = (n_{\mathrm{obs}} - n_{\mathrm{exp}})/n_{\mathrm{exp}}, \tag{8}$$

where n_{obs} and n_{exp} are the observed and expected number of galaxies within $2000\ \mathrm{km\,s^{-1}}$, respectively. We find an overdensity of $\delta = 2.4$ for companions with $\Delta v < 2000\ \mathrm{km\,s^{-1}}$. This increases to $\delta \approx 4.3$ for the companions with $\Delta v < 1000\ \mathrm{km\,s^{-1}}$. We stress that these overdensities are strict lower limits as it is expected that the majority of line candidates with $\Delta v > 2000\ \mathrm{km\,s^{-1}}$ are foreground CO lines and not high-redshift [C II] emitters (e.g., Decarli et al. 2020). In this case, it will lower n_{exp} in Equation (8) and thus increase δ. Our results therefore confirm and extend the clustering measurement by Decarli et al. (2017) based on a smaller sample of $z \sim 6$ quasars with companions.

5. Summary and Conclusions

We present a summary of the [C II] 158 μm emission line and underlying far-infrared continuum of 27 quasar host galaxies at $z \sim 6$ observed with ALMA at a spatial resolution of ~1 kpc. The sample covers about one-half of the quasars currently detected with ALMA in the [C II] emission at these redshifts, with a slight bias to the brighter sources in the complete sample: the mean (median) [C II] luminosity of our sample is 3×10^9 $(2.1 \times 10^9) L_{\odot}$, whereas that of all ALMA-detected quasars is 2.4×10^9 $(1.5 \times 10^9) L_{\odot}$. The spatial resolution of our sample allows us to spatially resolve the emission in the centers of the quasar host galaxies. We find that the [C II] emission in the quasar hosts has sizes between 1.0 and 4.8 kpc. We note that this holds for the bright centers of the galaxies and does not account for a more extended [C II] component that can only be quantified by stacking the emission of all quasars in our sample (Novak et al. 2020). The dust emission is more centrally concentrated than the [C II] in the central regions. Like in the case of [C II], a more extended faint dust component can only be recovered through stacking (Novak et al. 2020).

We find that 13 quasars (48%) have companion [C II]-emitting galaxies in the field (only considering candidates with a velocity difference up to $2000\ \mathrm{km\,s^{-1}}$), with distances between 3 and 88 kpc. We visually inspected the maps of the [C II] emission for nearby <5 kpc companion galaxies or irregular morphologies and conclude that at least eight quasar

hosts are undergoing a merger or have a disturbed [C II] morphology at the spatial scales probed by our observations.

Both the interstellar medium of the quasar host galaxies and their accreting supermassive black holes are thought to be located at the bottom of the potential wells of their respective dark matter halos. The high resolution of the ALMA observations, together with improved positions of the central accreting supermassive black holes based on Gaia DR2 corrections, now allow us to observationally test this hypothesis. We find that the interstellar medium and the central black holes are indeed cospatial (with offsets $\lesssim 0\farcs1$) in most cases. This suggests that the majority of the central black holes, as well as the interstellar medium, are located at the bottom of the gravitational wells of their respective dark matter halos. About $\sim$20% of the quasars are outliers with offsets up to $\sim$750 pc. This can be linked to disturbed morphologies in the [C II] emission, most likely due to ongoing or recent mergers (such interactions can displace the interstellar medium more easily than the central black holes). We find no correlation between the central surface brightness of the FIR emission and the bolometric luminosity of the (positionally coincident) accreting central supermassive black hole.

The star formation rate densities in the host galaxies, derived from the FIR measurements, peak at the galaxy centers and typically reach values between 100 and 1000 $M_\odot\,\mathrm{yr}^{-1}\,\mathrm{kpc}^{-2}$. These values are below the Eddington limit for star formation but are similar to those found in local ULIRGs. These star formation rate densities drop toward larger radii by typically an order of magnitude, reaching values that exceed those found in nearby galaxy disks. Likewise, the [C II]/FIR ratio is lowest in the centers of the quasar hosts, where luminosity ratios as low as a few times 10^{-4} are found, similar to studies of high-redshift starburst galaxies that show similar far-infrared surface brightness densities. Toward the outskirts of the disks, these values increase by a factor of a few, also reflecting the fact that the [C II] emission is typically more extended than the FIR continuum.

The observations presented here have typical on-source integration times of 0.5–1.5 hr with ALMA. The brightness of the targets imply that even higher resolution imaging of the quasar hosts, pushing to a resolution well below 1 kpc in the frame of the quasar host galaxies, is within reach (Venemans et al. 2019). Among other things, such studies would then allow one to probe the formation of massive galaxies in the early universe in detail and to investigate the interplay between emission from the accreting supermassive black hole and the interstellar medium down to scales of $<$100 pc.

We thank the referee for carefully reading the manuscript and providing constructive comments and suggestions. B.P.V., F.W., Ml.N., Ma.N., and A.B.D. acknowledge funding through the ERC Advanced Grant 740246 (Cosmic Gas). This paper makes use of the following ALMA data: ADS/JAO.ALMA#2012.1.00240.S, ADS/JAO.ALMA#2012.1.00882.S, ADS/JAO.ALMA#2013.1.00273.S, ADS/JAO.ALMA#2015.1.00399.S, ADS/JAO.ALMA#2015.1.00692.S, ADS/JAO.ALMA#2016.1.00544.S, ADS/JAO.ALMA#2016.A.000018.S, ADS/JAO.ALMA#2017.1.00396.S, ADS/JAO.ALMA#2017.1.01301.S, ADS/JAO.ALMA#2018.1.00908.S. ALMA is a partnership of ESO (representing its member states), NSF (USA), and NINS (Japan), together with NRC (Canada) and NSC and ASIAA (Taiwan), in cooperation with the Republic of Chile. The Joint ALMA Observatory is operated by ESO, AUI/NRAO, and NAOJ. This work has made use of data from the European Space Agency (ESA) mission Gaia (https://www.cosmos.esa.int/gaia), processed by the Gaia Data Processing and Analysis Consortium (DPAC, https://www.cosmos.esa.int/web/gaia/dpac/consortium). Funding for the DPAC has been provided by national institutions, in particular the institutions participating in the Gaia Multilateral Agreement.

Facility: ALMA.

Appendix A
Notes on Individual Objects

We summarize here some notes on individual objects, sorted by R.A.

A.1. P009–10

Quasar P009–10 was part of the ALMA Cycle 3 [C II] survey presented in Decarli et al. (2018) and is the most luminous [C II] source in our sample. Higher resolution imaging was obtained in Cycle 5. The source shows very extended [C II] emission with an estimated spatial FWHM of $4.9 \times 3.4\,\mathrm{kpc}^2$ based on a 2D fit to the [C II] map. This quasar has a disturbed [C II] morphology (Figure 3) and might undergo a merger with a very nearby source.

A.2. J0100+2802

This luminous quasar is powered by the most massive black hole currently known at $z \gtrsim 6$ of $>10^{10}\,M_\odot$ (Wu et al. 2015). Observations of FIR, [C II], and CO emission from the host galaxy were presented in Wang et al. (2016). The high-resolution data used in this paper were already presented in Wang et al. (2019). Our line search revealed a potential

Table 5
Newly Discovered Companion Galaxies in the Quasar Fields

Name	$z_{[\mathrm{CII}]}$	$L_{[\mathrm{CII}]}$ ($10^8\,L_\odot$)	L_{FIR} ($10^{11}\,L_\odot$)	Distance (kpc)	Δv (km s^{-1})
J0100+2802C1	6.3241 ± 0.0008	8.12 ± 1.36	<4.05	87.8	−110 ± 30
P183+05C1	6.4352 ± 0.0012	4.26 ± 1.28	8.13 ± 1.40	57.3	−140 ± 50
J1319+0950C2	6.1444 ± 0.0005	3.41 ± 0.77	3.78 ± 1.00	63.2	+410 ± 20
J1342+0928C1	7.5341 ± 0.0009	1.29 ± 0.39	1.69 ± 0.56	27.2	−210 ± 30
P231–20C1	6.5459 ± 0.0004	2.03 ± 0.48	<2.51	56.6	−1620 ± 20
J2054–0005C1	6.0383 ± 0.0003	5.28 ± 1.41	<9.05	77.3	−20 ± 10
J2318–3113C1	6.4095 ± 0.0003	0.92 ± 0.21	<1.33	31.5	−1340 ± 10
J2318–3113C2	6.4575 ± 0.0004	1.74 ± 0.48	<2.97	71.0	+590 ± 10
J2318–3029C1	6.1223 ± 0.0010	9.01 ± 2.08	6.61 ± 2.20	64.7	−980 ± 40

companion galaxy ∼90 kpc from the quasar (see Table 5 and the discussion in Section 4.4).

A.3. J0109–3047

The quasar J0109–3047 was imaged with ALMA in Cycle 1 (Venemans et al. 2016). The quasar was targeted at kiloparsec resolution twice, in Cycle 2 and Cycle 3. We combined the data from both cycles to create deeper maps. Interestingly, for this source, the rest-frame UV emission lines from the broad-line region near the accreting black hole show very large blueshifts compared to the systemic redshift of the quasar as traced by [C II], with the blueshifts among the largest found in high-redshift quasars (Venemans et al. 2016; Mazzucchelli et al. 2017). This could be due to an outflow or indicate that the accreting black hole is offset from the center of the host galaxy as traced by [C II] emission, due to, for example, a recent major merger. This latter scenario is strengthened by the ∼700 pc offset between the center of dust emission and the quasar (see Section 4.1 and Figure 5).

A.4. J0305–3150

Low-resolution [C II] observations of this quasar were published in Venemans et al. (2016). In ALMA Cycle 2 and Cycle 3, higher resolution observations were obtained. We combined the two high-resolution data sets in this paper. More recently, this quasar host was imaged at ∼400 pc (0.″07) resolution (Venemans et al. 2019). At 0.″07 resolution, the [C II] morphology is highly irregular, and several faint companion galaxies are located within a few kiloparsecs (Venemans et al. 2019). The brightness of the source in Table 2 is taken from the higher S/N data in Venemans et al. (2019). We here only include the ∼1 kpc resolution data for consistency. There are three companion [C II] emitters in the field, all within 40 kpc and 400 km s^{-1} of the quasar (Venemans et al. 2019). These line emitters were also found in our line search (Section 3.3). A fourth [C II] emission line candidate we discovered in this field is at least >3000 km s^{-1} away from the quasar and is likely not associated with it.

A.5. P065–26

The high-resolution FIR observations of quasar P065–26 show very extended [C II] emission (∼5 kpc; see Table 3). The emission has a disturbed morphology (Figure 3), an indication that the source is likely undergoing a merging event.

A.6. J0842+1218

In the field of this quasar, Decarli et al. (2017) reported a companion [C II] emitter at a distance of ∼47 kpc. The ∼0.″25 resolution follow-up imaging of the quasar and the companion was recently published by Neeleman et al. (2019). They also discovered a second, fainter companion about 31 kpc from the quasar, which was rediscovered in our blind search for line emitters in this field (see Section 3.3).

A.7. P167–13

The [C II] emission in this quasar at $z = 6.5$ was independently discovered by Willott et al. (2017) and Decarli et al. (2018). The 0.″5 imaging by Willott et al. (2017) showed that this quasar has a nearby companion (5 kpc from the quasar). This companion source was confirmed in higher-spatial-resolution ALMA data by Neeleman et al. (2019) and was also found in our blind line search (Section 3.3). The companion has also been detected in the rest-frame UV (Mazzucchelli et al. 2017) and possibly in X-rays (Vito et al. 2019).

A.8. J1120+0641

The FIR emission of the host galaxy was initially detected by the Plateau de Bure Interferometer (PdBI) and published in Venemans et al. (2012). Follow-up higher-spatial-resolution imaging of the [C II] line was obtained with ALMA in Cycle 1 (Venemans et al. 2017a). In Venemans et al. (2017a), a possible offset of 0.″5 between the accreting black hole and the host galaxy was reported. With the updated quasar position, derived by exploiting Gaia astrometry of nearby stars (Section 2.3) and listed in Table 1, the offset is now negligible (0.″03 ± 0.″04).

A.9. P183+05

The quasar P183+05 is the second brightest of our sample in both [C II] and dust emission. Our line search revealed two candidate line emitters in the field (Table 4), one of which is potentially a [C II]-emitting galaxy that is 140 km s^{-1} and 57 kpc from the quasar (Table 5).

A.10. J1306+0356

This source was part of the low-resolution ALMA survey of $z \sim 6$ quasar hosts published by Decarli et al. (2018). The low-resolution data showed that the quasar host is very extended, with a [C II] size >7 kpc (Decarli et al. 2018). High-resolution ALMA data revealed a more compact quasar host with a nearby (∼5 kpc) companion (Neeleman et al. 2019).

A.11. J1319+0950

This source was one of the first quasars imaged with ALMA in Cycle 0 (Wang et al. 2013). Higher-spatial-resolution 0.″3 observations were obtained in Cycle 1. The 0.″3 imaging of the [C II] emission showed a velocity gradient consistent with a rotating gas disk (Shao et al. 2017). Reanalysis of these data reveals a very close companion only ∼3 kpc from the quasar (see Figure 3). Another possible companion is located 63 kpc away (Table 5).

A.12. J1342+0928

This is currently the highest-redshift quasar known. The first detection of the [C II] and dust continuum emission from the host galaxy at $z = 7.54$ was made with NOEMA (Venemans et al. 2017b). The higher-spatial-resolution [C II] imaging with ALMA described in this paper was recently published by Bañados et al. (2019), who classify this object as a merger. In the data cube, we discovered a candidate [C II] emitter that is 27 kpc from the quasar (Tables 4 and 5).

A.13. P231–20

The quasar P231–20 at $z = 6.6$ has a gas-rich companion located 9 kpc from the quasar (Figure 3), which was originally discovered by Decarli et al. (2017). The high-spatial-resolution observations presented here were already analyzed by Neeleman et al. (2019). They reported the second, fainter [C II] companion at a distance of 14 kpc (see Table 4). A possible third companion is located 57 kpc and $\sim$1600 km s^{-1} from the quasar (Table 5). A fourth candidate line emitter is not associated with the quasar, based on the large velocity difference (>15,000 km s^{-1}).

A.14. P308–21

The [C II] emission of quasar P308–21 shows very extended tails, suggesting that this source is undergoing a merger (Decarli et al. 2017). The deep, high-resolution [C II] imaging of this quasar revealed a main emission component centered on the quasar and two extended components stretching $\sim$1500 km s^{-1} (Decarli et al. 2019). The [C II] kinematics and morphology can be explained by the tidal stripping of a satellite galaxy by the quasar host, confirming that the object is undergoing a merger (Decarli et al. 2019).

A.15. J2054–0005

The quasar J2054–0005 was first observed by ALMA in Cycle 0. The high-spatial-resolution data presented here were obtained in Cycle 5. Our line search returned a potential companion galaxy at the same redshift as the quasar located at a projected distance of 77 kpc.

A.16. J2100–1715

This is one of the sources that showed a FIR-bright companion at the same redshift in low-resolution data (Decarli et al. 2017). The distance on the sky between the quasar and the companion is 61 kpc (Decarli et al. 2017; Neeleman et al. 2019) and was rediscovered by our line search.

A.17. J2318–3113

Both [C II] and continuum emission of this quasar are very extended. The measured sizes are $\sim$5 kpc, although the S/N of the detections is relatively low (peak S/N $\sim$ 5–6). There are two potential companion galaxies in this quasar field (Table 5).

A.18. J2348–3054

Low-resolution [C II] observations of this quasar at $z = 6.9$ were obtained with ALMA in Cycle 1 and published by Venemans et al. (2016). Higher-spatial-resolution imaging was obtained in Cycle 2 and Cycle 3. Because of possible astrometric errors in the Cycle 2 data, we did not combine the data from the two ALMA cycles, and we here only present the observations obtained in Cycle 3. Both [C II] and dust emission are very compact, with deconvolved sizes <1 kpc.

Appendix B
Candidate [C II] Companions in the Quasar Fields

We present here the new candidate [C II] companions discussed in Section 4.4 and summarized in Table 5. These candidates were recovered in the blind line search and could potentially be [C II]-emitting galaxies within 2000 km s^{-1} of the quasar (Section 4.4). Single-pixel spectra, extracted at the peak of the candidate line emission, are shown toward the right in Figure 11. Of the three maps that are shown, the central one displays the candidate emission line collapsed over 1.2 × FWHM. The maps toward the left and the right show emission away from the center, as indicated by the gray regions in the spectra toward the right. Contours in the maps start at $\pm 2\sigma$ and increase in steps of 1σ; positive contours are shown as black lines, and negative contours as red lines. The synthesized beam sizes are given in the bottom left corner of the maps. Gaussian fits are shown as blue lines on top of the spectra. The apertures used to extract the total spectrum of the candidates are indicated with light green circles. The parameters of the Gaussian fit to the total spectra are listed in Table 4.

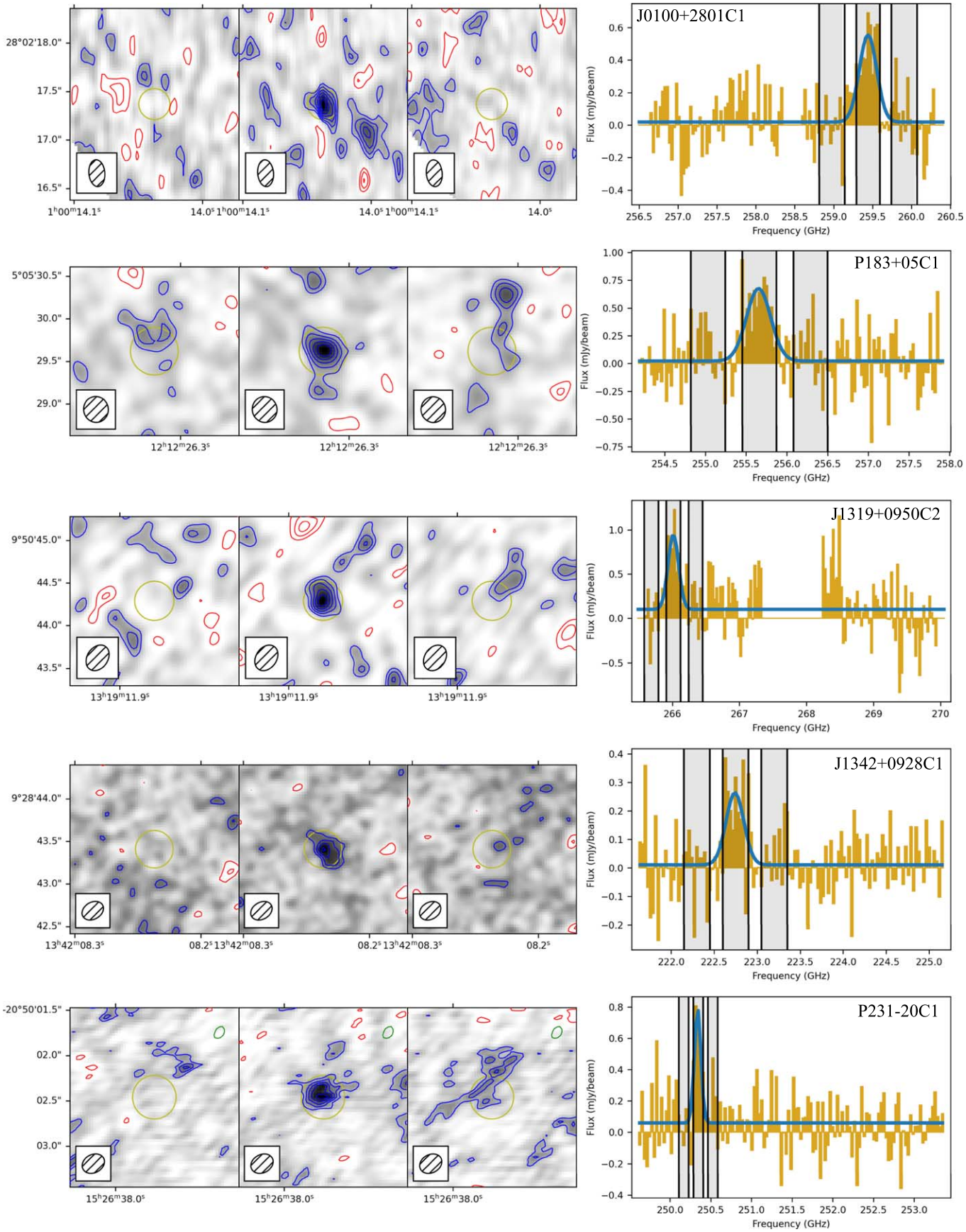

Figure 11. Maps and spectra of the new candidate [C II] companions found in the fields of the quasars, as discussed in Section 3.3 and listed in Table 5. See Appendix B for details.

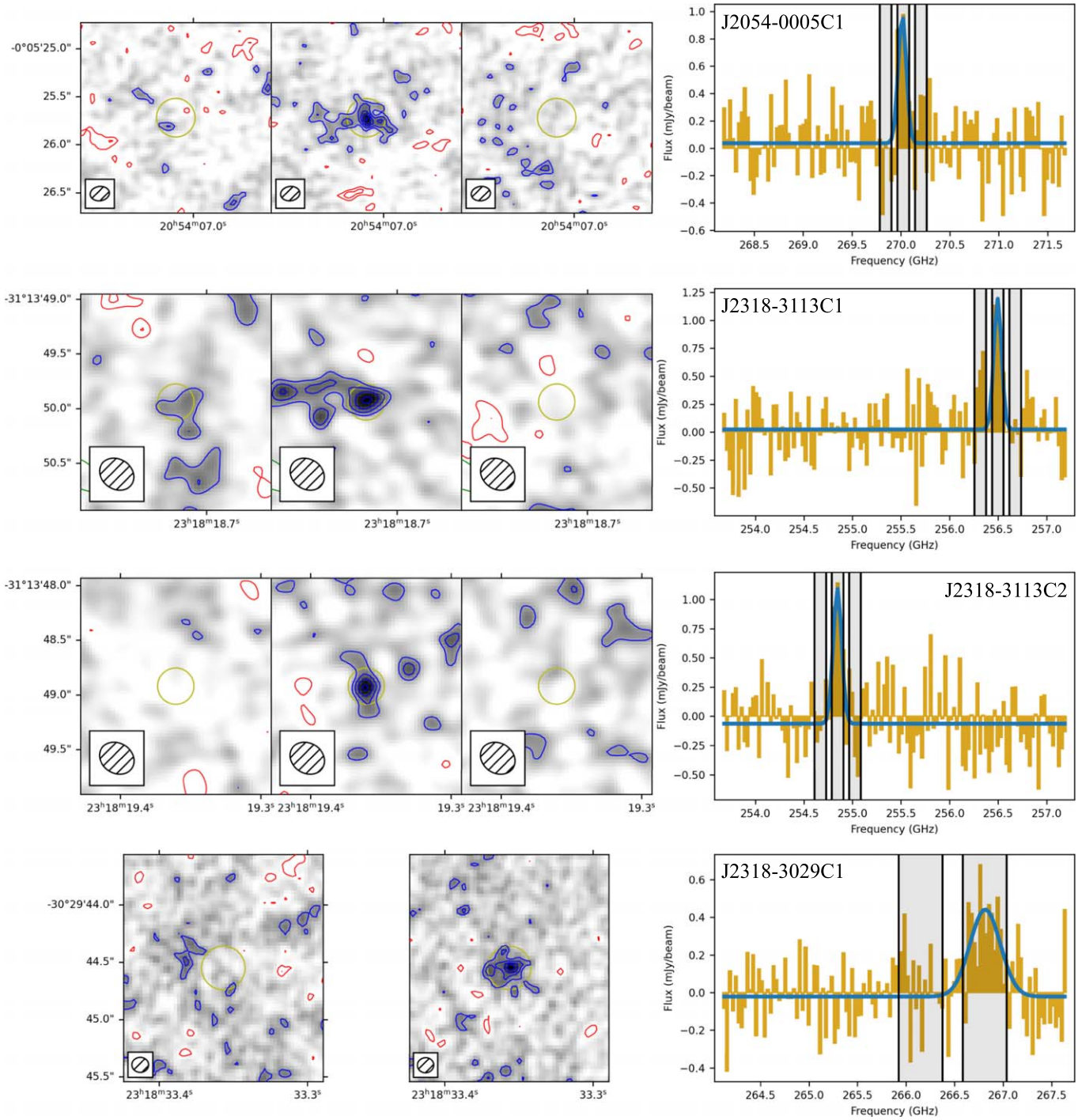

Figure 11. (Continued.)

ORCID iDs

Bram P. Venemans https://orcid.org/0000-0001-9024-8322
Fabian Walter https://orcid.org/0000-0003-4793-7880
Marcel Neeleman https://orcid.org/0000-0002-9838-8191
Mladen Novak https://orcid.org/0000-0001-8695-825X
Justin Otter https://orcid.org/0000-0003-3191-9039
Roberto Decarli https://orcid.org/0000-0002-2662-8803
Eduardo Bañados https://orcid.org/0000-0002-2931-7824
Alyssa Drake https://orcid.org/0000-0002-0174-3362
Emanuele Paolo Farina https://orcid.org/0000-0002-6822-2254
Melanie Kaasinen https://orcid.org/0000-0002-1173-2579
Chiara Mazzucchelli https://orcid.org/0000-0002-5941-5214
Chris Carilli https://orcid.org/0000-0001-6647-3861
Xiaohui Fan https://orcid.org/0000-0003-3310-0131
Hans-Walter Rix https://orcid.org/0000-0003-4996-9069
Ran Wang https://orcid.org/0000-0003-4956-5742

References

Bañados, E., Novak, M., Neeleman, M., et al. 2019, ApJL, 881, L23
Bañados, E., Venemans, B. P., Mazzucchelli, C., et al. 2018, Natur, 553, 473
Bartlett, D. J., Desmond, H., Devriendt, J., Ferreira, P. G., & Slyz, A. 2020, MNRAS, in press

Beelen, A., Cox, P., Benford, D. J., et al. 2006, ApJ, 642, 694
Capak, P. L., Carilli, C., Jones, G., et al. 2015, Natur, 522, 455
Chambers, K. C., Magnier, E. A., Metcalfe, N., et al. 2016, arXiv:1612.05560
Chanial, P., Flores, H., Guiderdoni, B., et al. 2007, A&A, 462, 81
da Cunha, E., Groves, B., Walter, F., et al. 2013, ApJ, 766, 13
De Rosa, G., Venemans, B. P., Decarli, R., et al. 2014, ApJ, 790, 145
Decarli, R., Aravena, M., Boogaard, L., et al. 2020, ApJ, 902, 110
Decarli, R., Dotti, M., Bañados, E., et al. 2019, ApJ, 880, 157
Decarli, R., Walter, F., Venemans, B. P., et al. 2017, Natur, 545, 457
Decarli, R., Walter, F., Venemans, B. P., et al. 2018, ApJ, 854, 97
Díaz-Santos, T., Armus, L., Charmandaris, V., et al. 2013, ApJ, 774, 68
Díaz-Santos, T., Armus, L., Charmandaris, V., et al. 2014, ApJL, 788, L17
Díaz-Santos, T., Armus, L., Charmandaris, V., et al. 2017, ApJ, 846, 32
Downes, D., & Solomon, P. M. 1998, ApJ, 507, 615
Edge, A., Sutherland, W., Kuijken, K., et al. 2013, Msngr, 154, 32
Ellison, S. L., Prochaska, J. X., Hennawi, J., et al. 2010, MNRAS, 406, 1435
Gaia Collaboration, Brown, A. G. A., Vallenari, A., et al. 2018, A&A, 616, A1
González-López, J., Decarli, R., Pavesi, R., et al. 2019, ApJ, 882, 139
Gullberg, B., Swinbank, A. M., Smail, I., et al. 2018, ApJ, 859, 12
Helou, G., Khan, I. R., Malek, L., & Boehmer, L. 1988, ApJS, 68, 151
Hennawi, J. F., Strauss, M. A., Oguri, M., et al. 2006, AJ, 131, 1
Herrera-Camus, R., Sturm, E., Graciá-Carpio, J., et al. 2018, ApJ, 861, 95
Hodge, J. A., Swinbank, A. M., Simpson, J. M., et al. 2016, ApJ, 833, 103
Kaczmarczik, M. C., Richards, G. T., Mehta, S. S., & Schlegel, D. J. 2009, AJ, 138, 19
Kennicutt, R. C., & Evans, N. J. 2012, ARA&A, 50, 531
Kroupa, P., & Weidner, C. 2003, ApJ, 598, 1076
Lamarche, C., Verma, A., Vishwas, A., et al. 2018, ApJ, 867, 140
Leipski, C., Meisenheimer, K., Walter, F., et al. 2014, ApJ, 785, 154
Leroy, A. K., Walter, F., Sandstrom, K., et al. 2013, AJ, 146, 19
Litke, K. C., Marrone, D. P., Spilker, J. S., et al. 2019, ApJ, 870, 80
Lutz, D., Berta, S., Contursi, A., et al. 2016, A&A, 591, A136
Marian, V., Jahnke, K., Mechtley, M., et al. 2019, ApJ, 882, 141
Mazzucchelli, C., Bañados, E., Venemans, B. P., et al. 2017, ApJ, 849, 91
McMullin, J. P., Waters, B., Schiebel, D., Young, W., & Golap, K. 2007, in ASP Conf. Ser., 376, Astronomical Data Analysis Software and Systems XVI, ed. R. A. Shaw, F. Hill, & D. J. Bell (San Francisco, CA: ASP), 127
Murphy, E. J., Condon, J. J., Schinnerer, E., et al. 2011, ApJ, 737, 67
Neeleman, M., Bañados, E., Walter, F., et al. 2019, ApJ, 882, 10
Nguyen, N. H., Lira, P., Trakhtenbrot, B., et al. 2020, ApJ, 895, 74
Novak, M., Bañados, E., Decarli, R., et al. 2019, ApJ, 881, 63
Novak, M., Venemans, B., Walter, F., et al. 2020, ApJ, 904, 131
Pensabene, A., Carniani, S., Perna, M., et al. 2020, A&A, 637, A84
Planck Collaboration, Ade, P. A. R., Aghanim, N., et al. 2016, A&A, 594, A13
Rybak, M., Calistro Rivera, G., Hodge, J. A., et al. 2019, ApJ, 876, 112
Rybak, M., Hodge, J. A., Vegetti, S., et al. 2020, MNRAS, 494, 5542
Sargsyan, L., Samsonyan, A., Lebouteiller, V., et al. 2014, ApJ, 790, 15
Schneider, R., Bianchi, S., Valiante, R., Risaliti, G., & Salvadori, S. 2015, A&A, 579, A60
Shao, Y., Wang, R., Jones, G. C., et al. 2017, ApJ, 845, 138
Shen, Y., Wu, J., Jiang, L., et al. 2019, ApJ, 873, 35
Smith, J. D. T., Croxall, K., Draine, B., et al. 2017, ApJ, 834, 5
Trakhtenbrot, B., Lira, P., Netzer, H., et al. 2017, ApJ, 836, 8
Venemans, B. P. 2006, AN, 327, 196
Venemans, B. P., Decarli, R., Walter, F., et al. 2018, ApJ, 866, 159
Venemans, B. P., McMahon, R. G., Walter, F., et al. 2012, ApJL, 751, L25
Venemans, B. P., Neeleman, M., Walter, F., et al. 2019, ApJ, 874, L30
Venemans, B. P., Röttgering, H. J. A., Miley, G. K., et al. 2007, A&A, 461, 823
Venemans, B. P., Walter, F., Decarli, R., et al. 2017a, ApJ, 837, 146
Venemans, B. P., Walter, F., Decarli, R., et al. 2017b, ApJL, 851, L8
Venemans, B. P., Walter, F., Zschaechner, L., et al. 2016, ApJ, 816, 37
Vito, F., Brandt, W. N., Bauer, F. E., et al. 2019, A&A, 628, L6
Walter, F., Riechers, D., Cox, P., et al. 2009, Natur, 457, 699
Wang, F., Wang, R., Fan, X., et al. 2019, ApJ, 880, 2
Wang, R., Wagg, J., Carilli, C. L., et al. 2011, ApJL, 739, L34
Wang, R., Wagg, J., Carilli, C. L., et al. 2013, ApJ, 773, 44
Wang, R., Wu, X.-B., Neri, R., et al. 2016, ApJ, 830, 53
Weinberger, R., Springel, V., Hernquist, L., et al. 2017, MNRAS, 465, 3291
Willott, C. J., Bergeron, J., & Omont, A. 2017, ApJ, 850, 108
Willott, C. J., Omont, A., & Bergeron, J. 2013, ApJ, 770, 13
Wu, X.-B., Wang, F., Fan, X., et al. 2015, Natur, 518, 512
Yang, J., Venemans, B., Wang, F., et al. 2019, ApJ, 880, 153
Yang, J., Wang, F., Fan, X., et al. 2020, ApJL, 897, L14